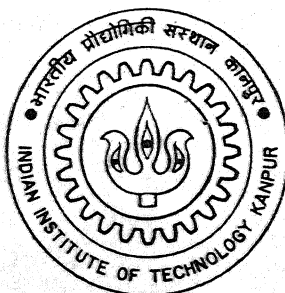# EXPERIMENTAL STUDIES ON FLOW AROUND CIRCULAR CYLINDERS

BY

VIVEK RAJAN SINGH

DEPARTMENT OF MECHANICAL ENGINEERING
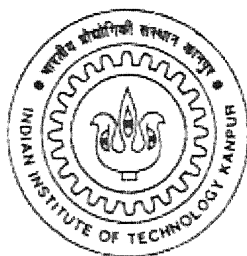
INDIAN INSTITUTE OF TECHNOLOGY KANPUR

AUGUST, 2000

Experimental Studies on Flow around Circular Cylinders

A Thesis Submitted
in Partial Fulfillment of the Requirements
for the Degree of

Master of Technology

by

Vivek Rajan Singh

Department of Mechanical Engineering
Indian Institute of Technology, Kanpur

Certificate

It is certified that the work contained in the thesis entitled **Experimental Studies on Flow around Circular Cylinders** by Mr. Vivek Rajan Singh has been carried out under our supervision and that this work has not been submitted elsewhere for a degree.

Gautam Biswas

Prof. Dr. Wolfgang Rodi
Institute for Hydromechanics
University of Karlsruhe
Karlsruhe-76128
Germany

Prof. Dr. Gautam Biswas
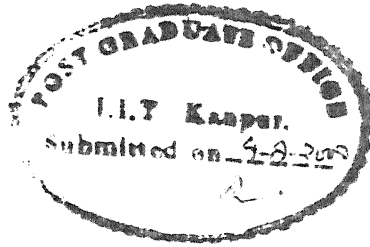Department of Mechanical Engineering
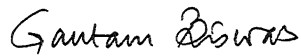Indian Institute of Technology
Kanpur-208016
India

Certificate

It is certified that the work contained in the thesis entitled **Experimental Studies on Flow around Circular Cylinders** by Mr. Vivek Rajan Singh has been carried out under our supervision and that this work has not been submitted elsewhere for a degree.

Prof. Dr. Wolfgang Rodi
Institute for Hydromechanics
University of Karlsruhe
Karlsruhe-76128
Germany

Prof. Dr. Gautam Biswas
Department of Mechanical Engineering
Indian Institute of Technology
Kanpur-208016
India

Abstract

Flow past a long circular cylinder has been widely investigated by the researchers. The dynamics of the wake and its dependance on the Reynolds number holds a lot of challenge as far as the physical understanding is concerned. With an increase in Reynolds number from a very low value, it is observed that the size of the separation bubbles increases. Gradually an asymmetry is created in the wake and further increase in Reynolds number causes vortex shedding to occur. The wake tends to become turbulent with multiple vortex shedding frequencies at a Reynolds number of 500.

The structure of flow past a short circular cylinder is markedly different from a long cylinder. The flow can be classified into three prominent regions i.e. the top region, the middle region and the base region. The top region is dominated by the flow over the free end and possesses a complex three dimensional structure. No vortex shedding occurs at the free end in contrast to the middle region where a disturbed vortex shedding is observed depending upon the cylinder aspect ratio. The base region exhibits the Karman vortex street alongwith the horseshoe vortex close to the base of the cylinder.

The present study is aimed at studying the wakes of both long and short circular cylinders. The Reynolds number for the flow is taken to be 22000. The flow field has been studied experimentally using a two component Laser Doppler Velocimeter(LDV) system. The quantities measured are the time mean velocities, the turbulent normal stresses and the turbulent shear stresses. Contour plots for these quantities have been presented alongwith the velocity vector plots for different horizontal planes. The differences as well as the similarities in the results for both the cases have been brought out.

Acknowledgements

Contents

List of Figures

Nomenclature

Regular Symbols

D	Cylinder diameter
f	Frequency of light scattered by the flow particle
l/d	Length to diameter ratio of the finite cylinder
n	Number of observations
p	Static pressure at the cylinder surface
p_∞	Static pressure at the inlet
Re	Reynolds Number
s	Fringe spacing of the interference pattern
T_u	Turbulence level in the oncoming flow
u_{ref}	Inlet flow velocity
$\overline{u}$	Time mean u-velocity
$\overline{u'^2}$	Streamwise turbulent normal stress
$\overline{u'v'}$	Turbulent shear stress
v	Velocity of flow
v_f	Drift velocity of the fringe system
$\overline{v}$	Time mean v-velocity
$\overline{v^2}$	Transverse turbulent normal stress
x	Coordinate along the flow direction
y	Coordinate in the transverse direction
z	Coordinate along the cylinder axis

Greek Symbols

α	Angle between the two interfering laser beams
β	Angle of incidence of the laser beam on the Bragg cell
λ	Wavelength of the laser
$\Delta\lambda$	Difference in wavelength between two interfering laser beams
λ_0	Wavelength of laser
λ_A	Wavelength of acoustic wave
μ	Refractive Index of the medium of the Bragg Cell
ρ	Density of the fluid
σ	Standard deviation
θ	Coordinate along the cylinder surface

Chapter 1

INTRODUCTION

1.1 Overview

Circular cylinders belong to a class of bodies which can be termed semi-aerodynamic, as compared to aerodynamic bodies such as aerofoils, and non-aerodynamic bodies with sharp edges such as square cylinders. Aerodynamic bodies have minimum or no separation, non-aerodynamic bodies have fixed separations at some of the corners. In the case of semi-aerodynamic bodies the position of separation varies depending on the magnitude of the approaching velocity and the flow profile, free stream turbulence, geometry, and surface roughness. The flow of an incompressible fluid around a circular cylinder is one of the most challenging problems in aerodynamics, considering both theory and physical phenomena. Fage et al. (1930) investigated the effect of free stream turbulence and surface roughness on the drag and on the pressure distribution around a circular cylinder. Roshko (1961) performed experiments in a pressurized wind tunnel and based on that he argued that a laminar separation bubble with turbulent reattachment, occuring in the supercritical Reynolds number range, disappears with increasing Re. He defined this as the transcritical range in which the separation itself was turbulent. Inline with Roshko's finding, Achenbach (1968) proved the existence of a separation bubble in the supercritical range using wall shear stress measurements. Dryden and Hill (1930) did full scale measurements in natural wind in

order to extend the experimental evidence to very high Reynolds numbers.

The phenomenon of vortex shedding behind bluff bodies has been investigated both experimentally and theoretically by different research workers. Extensive reviews of this topic have been given by Wille (1960), Morkovin (1964), Mair et al. (1971), Berger et al. (1972) and Bearman et al. (1980). A detailed experimental investigation has been carried out by Cantwell and Coles (1983) in the near wake of a circular cylinder at a Reynolds number of 140000. They used the flying hot-wire technique to conditionally sample the data on the basis of phase alignment thereby obtaining a series of phase-averaged results. An important conclusion made by them is that most of the turbulence production is concentrated near the the saddles and that vortex stretching at the intermediate scales is the primary mechanism of turbulence production.

The wake of a short circular cylinder with a free end possesses an enormous three dimensional complexity. It exhibits a markedly different behaviour as compared to the long cylinder, which has received ample attention of the researchers. Wieselsberger (1922) measurerd the drag coefficient of a circular cylinder having a finite height with its ends immersed in uniform stream. The results due to Wieselberger were employed for a long time to estimate the wind drag on a telegraph pole or a chimney. Dryden and Hill (1930) conducted experiments on a full scale chimney in the natural wind and also on a chimney model in a wind tunnel. They measured the pressure distributions over the chimney and found that the local drag coefficient has its maximum value in the neighbourhood of the free end of the chimney. Apart from the estimations about the drag on the finite height cylinder, the frequency of vortex shedding behind it is also very important for the design of chimneys, buildings etc. Initially, when no data was available on the frequency of vortex shedding behind a finite height cylinder, the data from an infinite cylinder were being used in place. Gould et al. (1968) also measured the distribution of the local drag coefficient of a chimney. Okamoto and Yagita

(1973) conducted extensive experiments on the flow past finite height circular cylinder placed normal to a plane surface. They studied the effect of the free end by comparing the results with those of an infinite circular cylinder. They found that with a decrease in the l/d(length to diameter) ratio of the cylinder the separation point moves forward. Also, the vortex shedding frequency was found to decrease as the free end of the cylinder was approached for aspect ratios $l/d \geq 7$. The vortex shedding frequency was found to decrease greatly with a decreasing l/d ratio. They also observed that one end of each vortex filament of the vortex street attaches to the rear side of the cylinder close to the free end and the other end attaches to the flat plate behind the cylinder. Taniguchi et al. (1981) estimated the pressure drag coefficient from the static pressure measurements of a finite cylinder immersed in a turbulent boundary layer. They also carried out some flow visualisation studies on the finite cylinder. Some other flow visualisation experiments along with measurements of surface pressure, Strouhal number etc. on a finite circular cylinder were carried out by Kawamura et al. (1984). They observed that the finite height circular cylinder possesses a smaller drag coefficient than a two-dimensional circular cylinder. The reason given was mainly due to the decrease of the separation velocity of the side wall flow. They also observed a pair of longitudinal vortices (trailing vortices) arising from the rear of the cylinder, immediately downstream of the free end. This they concluded was due to the coupling of the downwash flow from the free-end and the separated up-wash flow along the side wall. It was observed that the formation of a vortex street was inhibited in the free end region. The wake flow in this region was dominated by the down wash and the trailing vortex. They also concluded that below a certain aspect ratio l/d, no periodic vortex shedding occurs. The physical explanation given was that the free end region in that case extended all the way to the base. Hölscher and Niemann (1987) did flow visulization studies on the flow around a surface mounted circular cylinder. They observed two reverse flow vortices, in

the upstream separation region at the ground plate. One of these vortices was identified as the horse shoe vortex, which wraps itself around the body and then trails downstream. On the cylinder top, they found a sickle shaped flow region with a large lateral flow component. Separation occured at the leading edge and the two vortices with opposite sign were seen. They also noticed that the flow reattaches at the cylinder top and reverse flow occured in the separated region. An obvious conclusion was made by them that the material out of the leading edge separation region and out of the reverse flow region was being dragged along by the lateral flow around the cylinder tip.

1.2 Motivation

A large database of information exists on the flow past long cylinders. However, not much work has been done on the flow past a circular cylinder of finite height placed normally on a plane surface. In the present work we attempt to study the flow past a cylinder of finite height and compare it with the case of a long cylinder. The engineering applications of this configuration are flows across buildings, chimneys, towers or other wind sensitive structures and the flow across a pin fin as a means of augmenting heat transfer. In order to facilitate the design process of the above-mentioned structures we need to know about the pressure distribution and the wind drag data beforehand. Another important aspect which is to be taken into consideration is the frequency of vortex shedding, which is crucial for controlling the flutter of the structure. Furthermore, the study of the turbulent wake of a finite cylinder is also important as it addresses the problems of air pollution from a chimney or from a building. The study of the dynamics of the wake will also help us in predicting the diffusion of the pollutants in the wake of the chimney.

An experimental investigation is a reliable way of understanding the dynamics of such three-dimensional turbulent flows. Another important aspect of such ex-

perimental investigations is that they serve as a convenient tool for the evaluation of the results of numerical simulations.

Chapter 2

Experimental Set-Up and Conditions

The experiments were carried out in a closed water channel with a cross-section of $0.39 \times 0.56m$, supplied by a constant head tank. The flow situation and the coordinate system for both the infinite and finite cylinders are shown in Figs. 1 and 2. The origin of the coordinate system for the infinite cylinder lies at the cylinder centre and in the mid-plane (i.e. halfway along the height of the cylinder). Figure 1 shows the set-up for the infinite cylinder. The measurements were made at the mid plane as shown in the figure. Figure 2 depicts the set-up for the finite height cylinder having a length to diameter (l/d) ratio of 5. The origin of the coordinate system lies at the cylinder centre in the plane containing the free end. Measurements were made for two horizontal planes, one containing the free end, i.e. at $z = 0$ and the other one was at $z = -40mm$. From volume flux measurements and from the velocity profiles measured with the LDV, the average approach flow velocity was determined to be $u_{\mathrm{ref}} = 0.54m/s$ and the turbulence level in the oncoming flow was $T_u = \sqrt{\overline{u'^2}}/u_{ref}$ of 0.03.

2.1 The Laser Doppler Velocimeter system

The LDV system used here is a two component system operating in a forward

cylinder   test section

measurement
plane

392

Flow

x

y

560
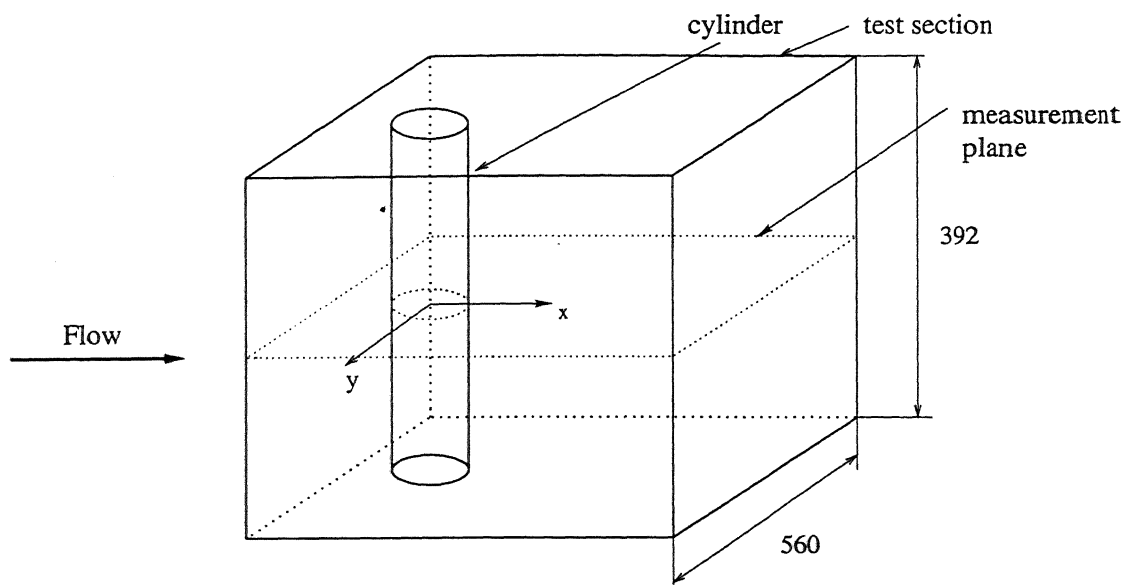
Fig.1   The Test Section fitted with the Infinite Cylinder

test section

measurement
planes

392

cylinder

Flow

z

x

y

200

560
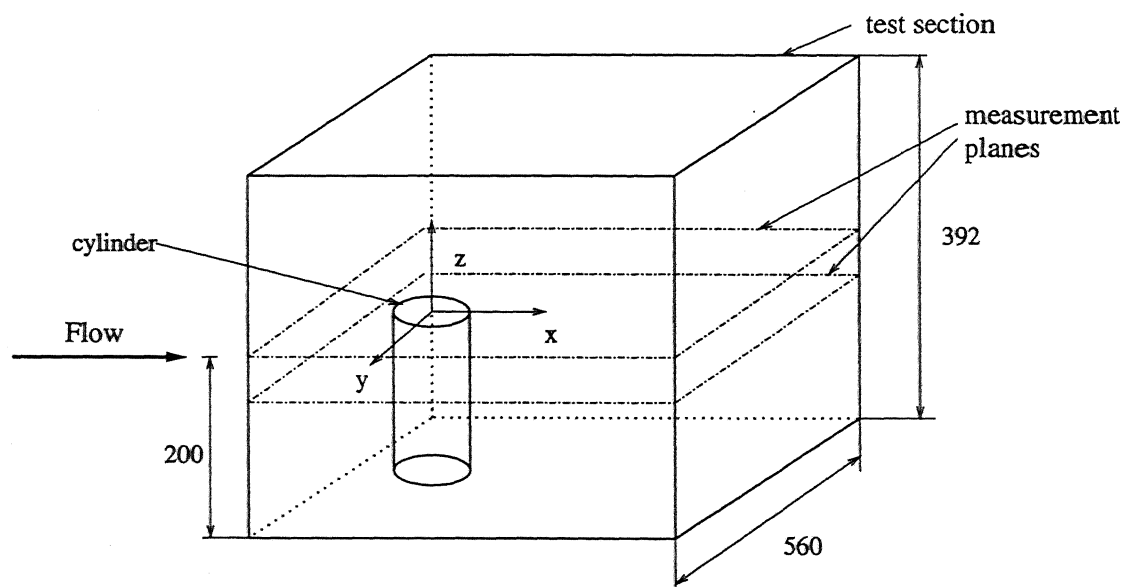
Fig.2   The Test Section fitted with the Finite Height Cylinder

-scatter interference fringe mode. We also call this the Differential Doppler Tech-
-nique. It uses an arrangement of Bragg cells as shown in Fig. 3. The two illumi-
nating beams derived from the laser are focussed into a small region by a single
lens. The beams are inclined at an angle α as shown in Fig. 4. An interference
pattern consisting of alternate bright and dark fringes results at the region at
the intersection of the two beams. A particle passing through the region scatters
light at a frequency proportional to its velocity. In order to estimate the velocity
of the flow, we first need to know the fringe spacing 's'. Figure 5. shows the

Fig.3   A Simple LDV System

8

-scatter interference fringe mode. We also call this the Differential Doppler Tech-
-nique. It uses an arrangement of Bragg cells as shown in Fig. 3. The two illumi-
nating beams derived from the laser are focussed into a small region by a single
lens. The beams are inclined at an angle α as shown in Fig. 4. An interference
pattern consisting of alternate bright and dark fringes results at the region at
the intersection of the two beams. A particle passing through the region scatters
light at a frequency proportional to its velocity. In order to estimate the velocity
of the flow, we first need to know the fringe spacing 's'. Figure 5. shows the

Fig.3   A Simple LDV System

Fig.4　Interference Fringe Pattern of Laser Beams

detailed diagram of the interference region. Planes of equal phase (wavefronts) separated by one wavelength are shown, and are named as X1, X2,...., Y1, Y2,...., etc. Z1, Z2,... etc are the planes on which the wavefronts associated with each beam intersect. The distance between these bright fringes is denoted as s. If we consider the right-angled triangle ABC as constructed in Fig. 5, we can easily arrive at the following formula for the fringe spacing s :

$$s \ = \ \frac{\lambda}{2\sin(\alpha/2)}$$

9

where

$$\lambda \equiv \text{wavelength of light}$$

$$\alpha \equiv \text{angle between the two interfering beams}$$

The expression for the frequency of light f scattered by a flow particle, in terms of the particle velocity v and the fringe spacing s is:

$$f = \frac{v}{s}$$

or

$$f = \frac{2v \sin (\alpha/2)}{\lambda}$$

This frequency 'f' is also called the differential Doppler frequency. This is the reason why this technique is sometimes called the 'intensity modulation' or 'real fringe' method.

It is important to note that the frequency is independent of the direction of reception. Thus, increasing the aperture of reception does not result in the broadening of the spectrum as it does in the reference beam technique. Also, if the two scattered beams are generated by one individual particle, their source is the same and there is no coherence limitation on the receiver. Thus a larger detector aperture can be used with advantage, yielding to larger signal amplitudes compared to the reference beam technique.

2.1.1   Frequency Shifting

Shifting the frequency of light beams is the most commonly used technique for directional discrimination of the flow. In the differential Doppler system, it is necessary to produce a frequency difference between the two beams incident on the scattering volume. This may be done by frequency shifting one beam or, more
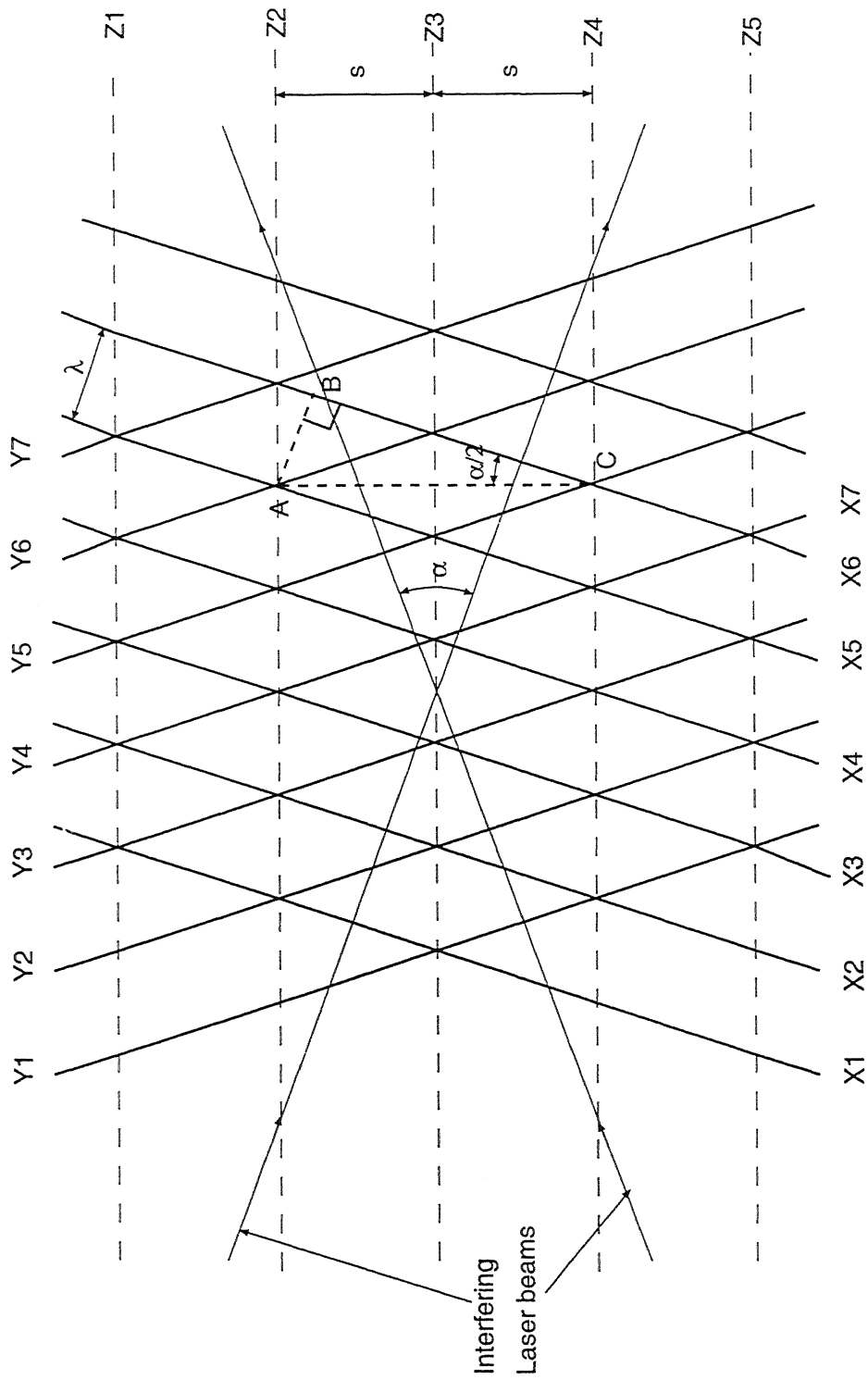
Fig.5   Diagram showing the geometry of Interference Fringe Pattern

usually, both so that a moving system of fringes is obtained. In the present investigation we have shifted both beams up but the magnitude of shifts are slightly different. The moving fringe pattern is illustrated in Fig. 6. A particle at rest within the interference region thus scatters light at a frequency equal to the shift frequency. Now if the particle is moving in the same direction as the fringes, the scattered light has a lower frequency. Similarly the frequency of the scattered light is raised when the particle is moving in the opposite direction.
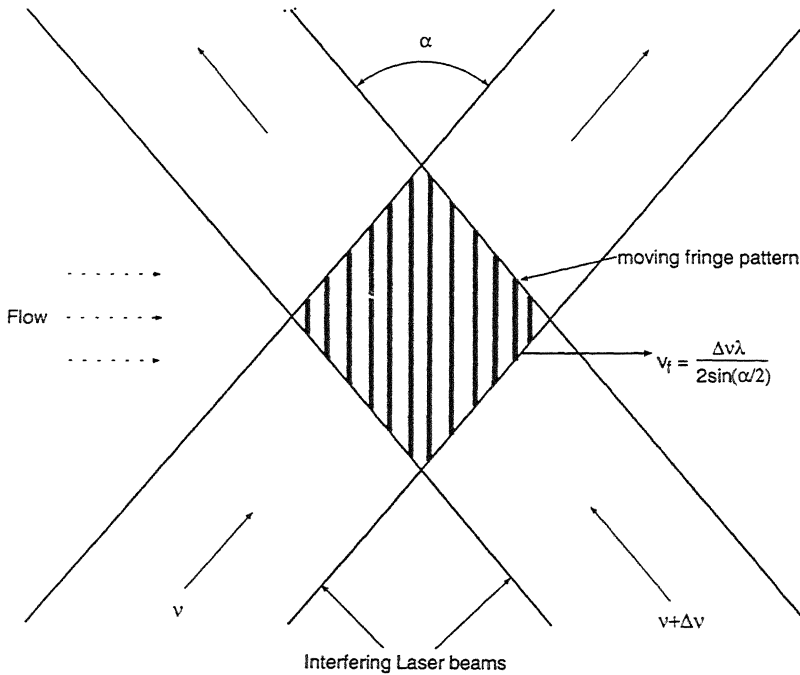
Fig.6 Moving Fringe Pattern formed by the crossing of two beams of different frequencies

The expression for the drift velocity v_f of the fringe system is:

$$v_f \;=\; \frac{\Delta\lambda}{2\sin{(\alpha/2)}}$$

2.1.2 Bragg Cells

Bragg cells are actually acousto-optic cells which produce a frequency shift in light by means of diffraction by acoustic waves. Whenever acoustic waves of suitable wavelength are passed through a transparent medium, they set up alternate layers of compression and rarefaction. These layers have slightly different refractive indices forming a three-dimensional diffraction grating. But since the changes in the local refractive index are very small, the diffraction efficiency is poor, except for certain angles of incidence and reflection.

To explain this phenomenon we consider the 'diffraction effect' of a plane acoustic wave as a combination of reflections from planes separating layers of slightly different refractive indices, μ and $\mu + \delta\mu$ (See Fig. 7). If the angle of incidence β, is such that whole of reflections reinforce by interference, the outcoming reflected beam is highly enhanced. This angle of incidence is called Bragg angle. The expression for Bragg angle is :

$$2\mu\lambda_A \cos\beta \;=\; \lambda_0$$

where

$\lambda_0 \equiv$ wavelength of light

$\lambda_A \equiv$ wavelength of acoustic wave

We know that shifting the acoustic waves by one wavelength causes a shift of one optical wavelength in the reflected beams. Therefore, the frequency shift of the reflected waves is simply equal to the frequency of the acoustic waves. The sign of the frequency shift can be positive or negative depending upon the direction of propagation of acoustic waves.
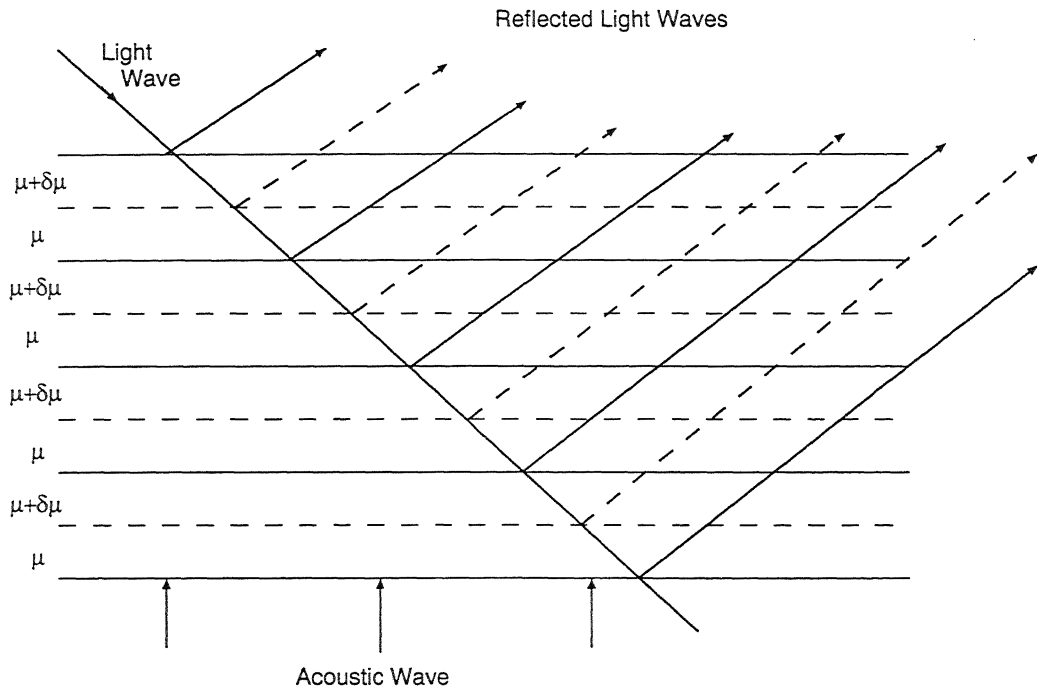
Fig.7 Principle of a Bragg Cell

A simple arrangement for frequency shifting using an acousto-optic cell is shown in Fig. 8. A laser beam is made to pass through a cell containing material in which acoustic waves are travelling. The acoustic waves are excited by a suitable piezometric transducer. Diffracted beams are produced as from a moving diffraction grating, but by orienting the cell to the Bragg angle most of the light can be concentrated in the +1 order of diffraction which then becomes the Bragg reflection.

Deviation of the shifted beam is usually undesirable, so two half prisms are

placed in front and behind the acoustic cell unit in order to return the beam to its original direction. We see that several beams emerge out of the bragg cell and each beam is having a different frequency shift (See Fig. 8). The beam which doesn't undergo any frequeency shift is called the zero order beam. The beam whose frequency is shifted by an amount prescribed by the Bragg's principle f_{Bragg}, is called the first order beam. Similarly, the second order beam is the one which undergoes a frequency shift equal to twice that of the first order beam. In the same way we have other higher order beams. But for our purpose, we block out all the other beams except the first order one.

2.1.3   The Probe Volume

The region consisting the fringes, where the crossing of the two laser beams takes place is called the 'probe volume', 'control volume' or 'scattering volume'. A particle moving in the probe volume produces a signal proportional to the modulated component of the intensity distribution. For precisely intersecting Gaussian beams of equal width, the contours of equal fringe amplitude are ellipsoids having their centers at the central cross-over point. A conventional defination of the limit of the probe volume is the contour corresponding to a fringe amplitude $1/e^2$ of its maximum value.

At low particle densities in the differential Doppler system, it is very important that the two light beams cross, overlapping as much as possible. For instance if there is only one particle the possibility of having a burst signal is very less unless it passes through the control volume. Alignment in the differential Doppler technique is even more important compared to the reference beam technique.

2.2   The Test Rig

The test rig consists of a laser tube to produce the laser beam, a series of optics to direct the laser beam in a desired manner, photomultiplier tubes and other

Second Order beam

First Order beam

Zero Order beam

Frequency shifted
beams

Prism

R.F.
Generator

Absorber

Piezoelectric
Transducer
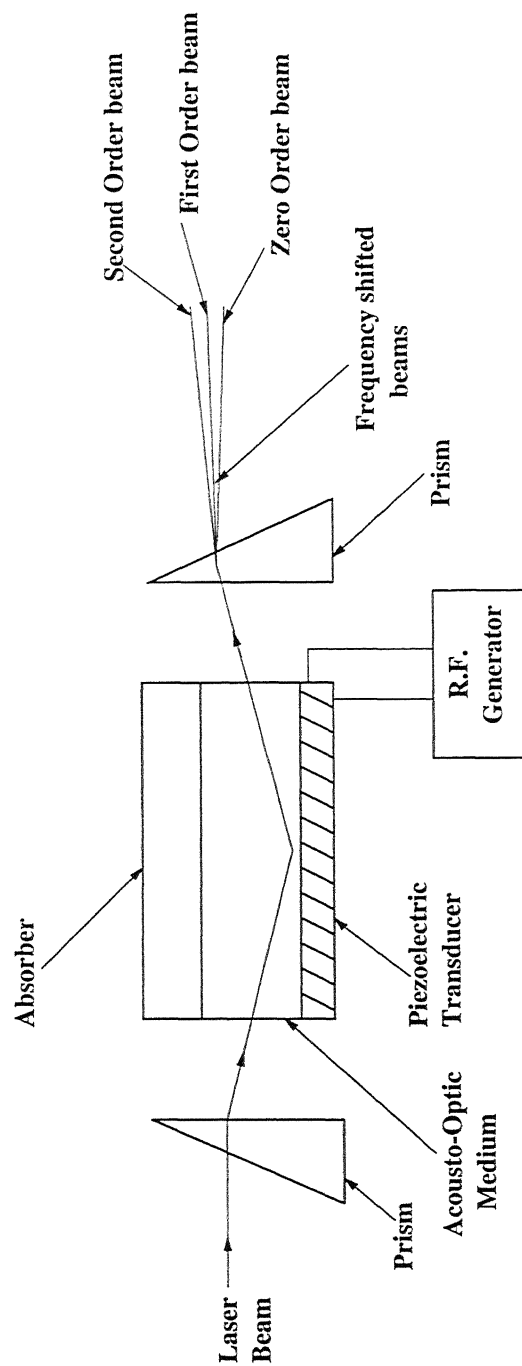
Acousto-Optic
Medium

Prism

Laser
Beam

Fig.8　Frequency Shifting of Light Beam by Bragg Cell

signal conditioning equipment. The schematic diagram of the test rig is shown in Fig. 9. The laser-tube produces a single laser beam which we will refer as the primary beam. Since two components of the velocities are to be measured, we use beams of two different colours. For this purpose we first separate the primary beam into three parallel beams, using a beam-splitter as shown in the Fig. 9. Then we perform optical filtering on all the three beams. Blue beam filters are used on the two outer beams which allow only the blue light to pass through. Similarly the middle beam is filtered through the green filter which allows only the green light to pass through. Then the two blue beams are made to pass through a pair of Bragg cells. This is done to introduce frequency shifts in both the beams. Again a beam splitter is used to separate the green beam into two parallel beams. Likewise we use a pair of Bragg cells on the green beams to produce frequency shifts. In order to measure the frequency shifts we use a digital frequency counter. The frequency shifted green and blue beams, which are four in number, are made to convege through a convex lens.

The test section is made up of glass, as it is required to be optically accessible. The laser-tube and whole of the optics is placed on a table below the closed water channel. In order to reflect the beams through the test section we introduce an inclined mirror in the path of the four converging beams. The four beams then meet at some point inside the test section. This is the point at which the flow velocity measurement is made. To analyse the flow, we have to make measurements in an entire array of points (the resolution depends upon the region of flow being investigated). For this reason the laser-tube and the entire optics is mounted on a table which can move freely in the horizontal plane. On the top of the test-section there is another inclined mirror which reflects the light beams coming up in the horizontal direction. A converging lens is again placed in the path of the diverging beams. Finally, there are photomultiplier tubes which converts the

optical bursts into electrical signals. The primary beams, which are four in number, are blocked out and only the scattered light is allowed to pass through. This is done because it is the scattered light which contains information about the flow velocity. Moreover the high intensity unscattered laser beams might damage the photomultiplier tubes. The scattered light is detected by the photomultiplier, whose output signal is fed into the amplifier. Infact there are two photomultiplier tubes, one each for both green and blue burst signals. The scattered light is made to pass through a semi-transparent mirror, which transmits a part of the scattered light towards the blue photomultiplier tube and reflects the remaining towards the green photomultiplier tube. Both the photomultiplier tubes have filters placed before them in order to allow light of only one wavelength to pass through(See Fig. 9).

In order to condition the signal, we use filters which perform bandpass filtering to filter both high and low frequency components off the signal. The conditioned signal is then fed into the computer for data acquisition.

2.3   Data Acquisition and Signal Processing

The burst signals generated by the photomultiplier tube have to be conditioned before final data acquisition. Since the signal is weak we have to amplify it before further processing. After amplification we need to condition the signal i.e. filter off both high and low frequency components. For this purpose we employ filters which perform 'bandpass filtering' on the signal. Bandpass Filtering is actually a combination of both High and Low Pass Filtering as shown in Fig. 11. Low Pass Filtering chops off the high frequency component i.e. the noise from the signal. Similarly high pass filtering removes the low frequencies from the signal. The low frequency portion of the signal arrives from the intensity variation of the laser beams, which as we know is gaussian. The amplified and filtered signal goes to the computer for further processing.
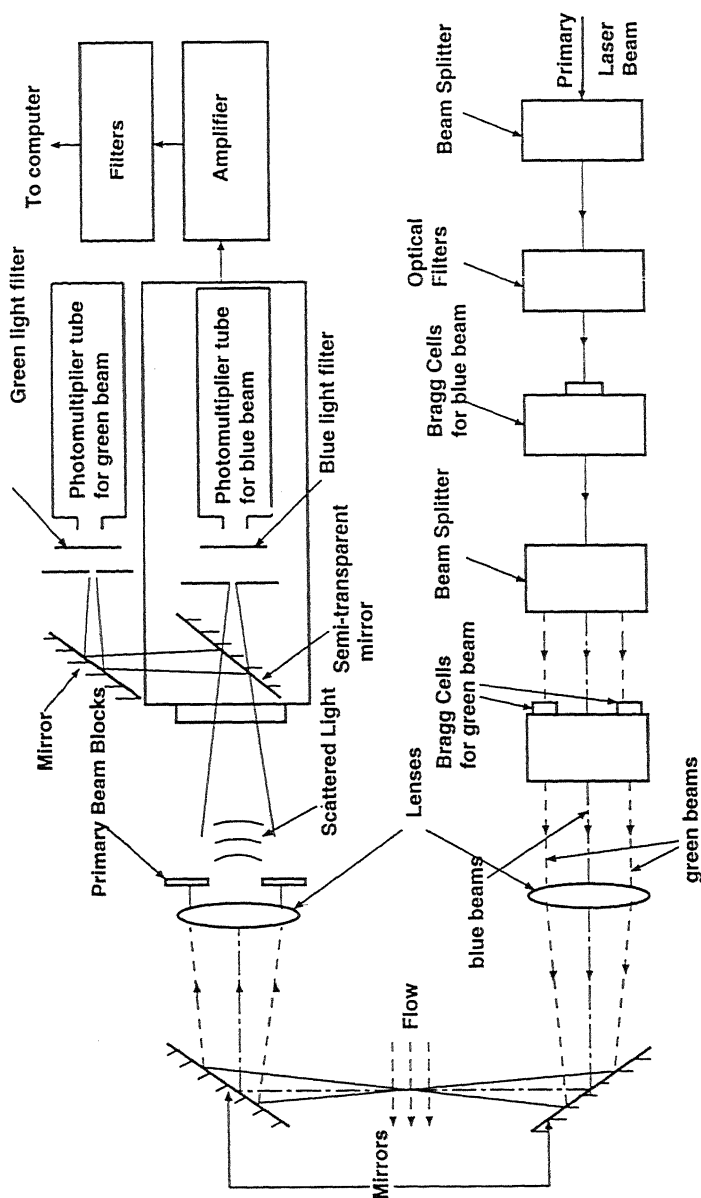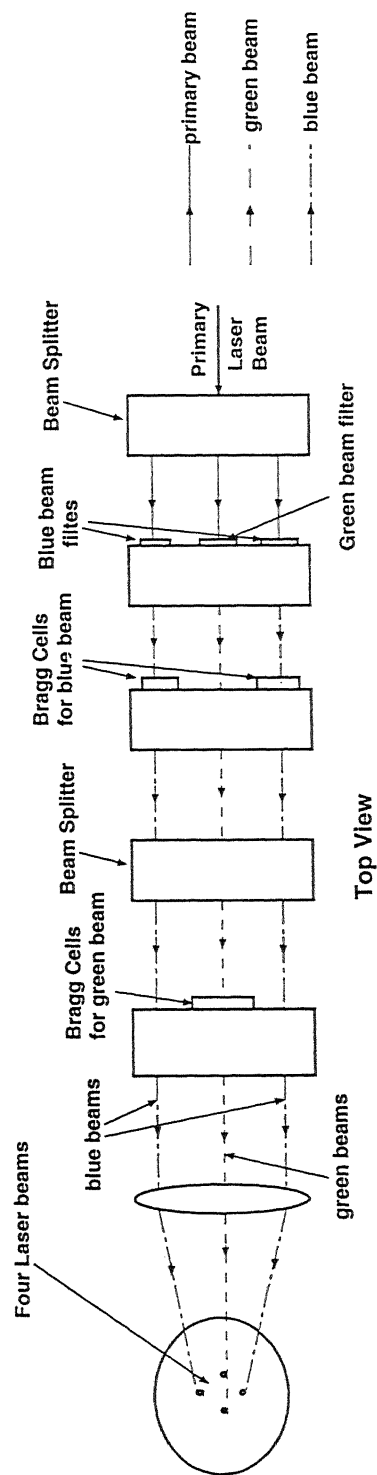
Fig.9   The Test Rig

The flow diagram of the signal processing inside the computer is shown in Fig. 12. A computer program has been written which takes different parameters which are critical for data processing, as input. Data acquisition starts when the amplitude of the blue burst signal reaches the trigger level. It then takes a Window FFT of the acquired signals. In our case we used a Hanning Window. Proceeding further, the height and the position of the peak for the blue signal is determined from the Power Spectrum. If the peak height is greater than a certain specified value, the peak is characterized as good and the program proceeds to determine the height and position of the peak for the green signal. If the green signal peak is also good, the velocities u and v are calculated. This is done simply by using the positions of both blue and green signal peaks. The peak position of the blue signal gives the u component of velocity and the peak position of the green signal gives the v component. These values are the instantenous values of velocities at a point. Our computer program takes a large number of such observations $(2000 - 4000)$ at the same point. It then averages out all the velocity observations to estimate the mean velocities at that point i.e. $\bar{u}$ and $\bar{v}$. Also other turbulent quantities like the turbulent normal stresses $(\overline{u'^2}$ and $\overline{v'^2})$ and the turbulent shear stress $(\overline{u'v'})$ are estimated. Depending upon the region of flow we have to vary the number of observations to be taken. High turbulence regions like the near wake, where standard deviations of both u and v velocities are high, require more number of observations to be taken. The regions where turbulence levels are low like the inflow region require lesser number of observations.

2.4 Applications and Advantages of LDV

LDV finds extensive applications in the field of turbulence research. Very often, for design applications in wind tunnels and in some actual flow situations, the velocity and turbulence profiles are needed. It is here that the LDV technique is very useful and enables detailed flow information to be obtained quickly. LDV
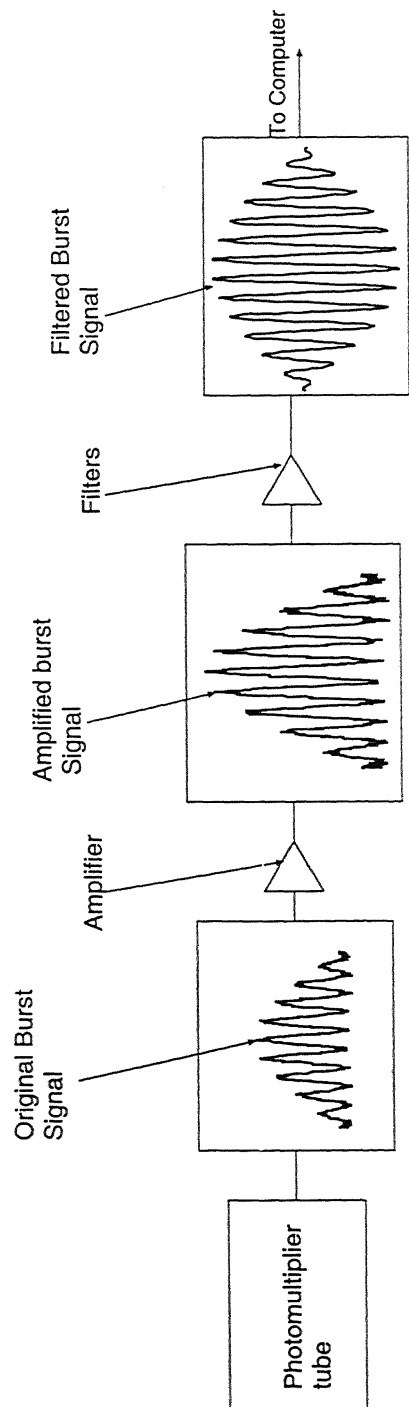
Fig.10 Analog part of Signal Processing

21

also finds applications in flows involving corrosive liquids or flames, since it dispenses with the use of material probes for flow measurements.

LDV offers a number of advantages over conventional methods of flow measurement. The most important one is that there is no obstruction to the flow while performing the measurements. Moreover, a very high optical resolution is obtainable with an LDV system. The reason for this is that the laser beams can be focussed into a very small volume in the region where the velocity is to be measured. LDV possesses a linear response and can cover a wide range of flow velocities from millimeters per second to supersonic. Another advantage of LDV is that it possesses a fast response and rapid fluctuations from turbulence can be followed. Also the LDV measurements are not affected by temperature unless unusually long light paths through hot gases are involved.

2.5 Sources of Error

It is necessary to account for the errors in any experimental investigation. There are two types of errors which are present in our measurements: (i) Systematic Errors (ii) Statistical Errors

Systematic Errors might be introduced into the readings due to various factors. First, the measurement of shift frequency might have some error in it. Secondly there are alignment errors. We know that alignment of optics is very crucial in the LDV technique and even a slight misalignment can introduce a significant error in the measurements. Thirdly the data acquisition part, which involves amplification, filtering and final acquisition, can also lead to some errors creeping into the system.

The Stastistical Errors are the errors introduced due to the process of averaging a large number of readings. The Statistical error is numerically equal to the standard deviation divided by the square root of the number of observations
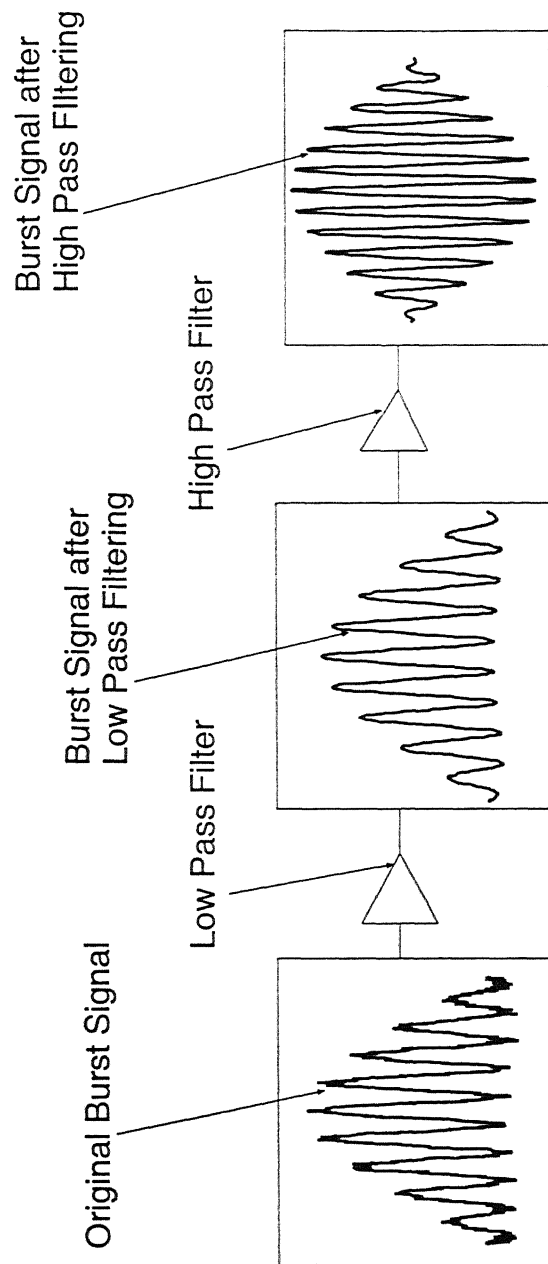
Fig.11   The Details of Filtering Process
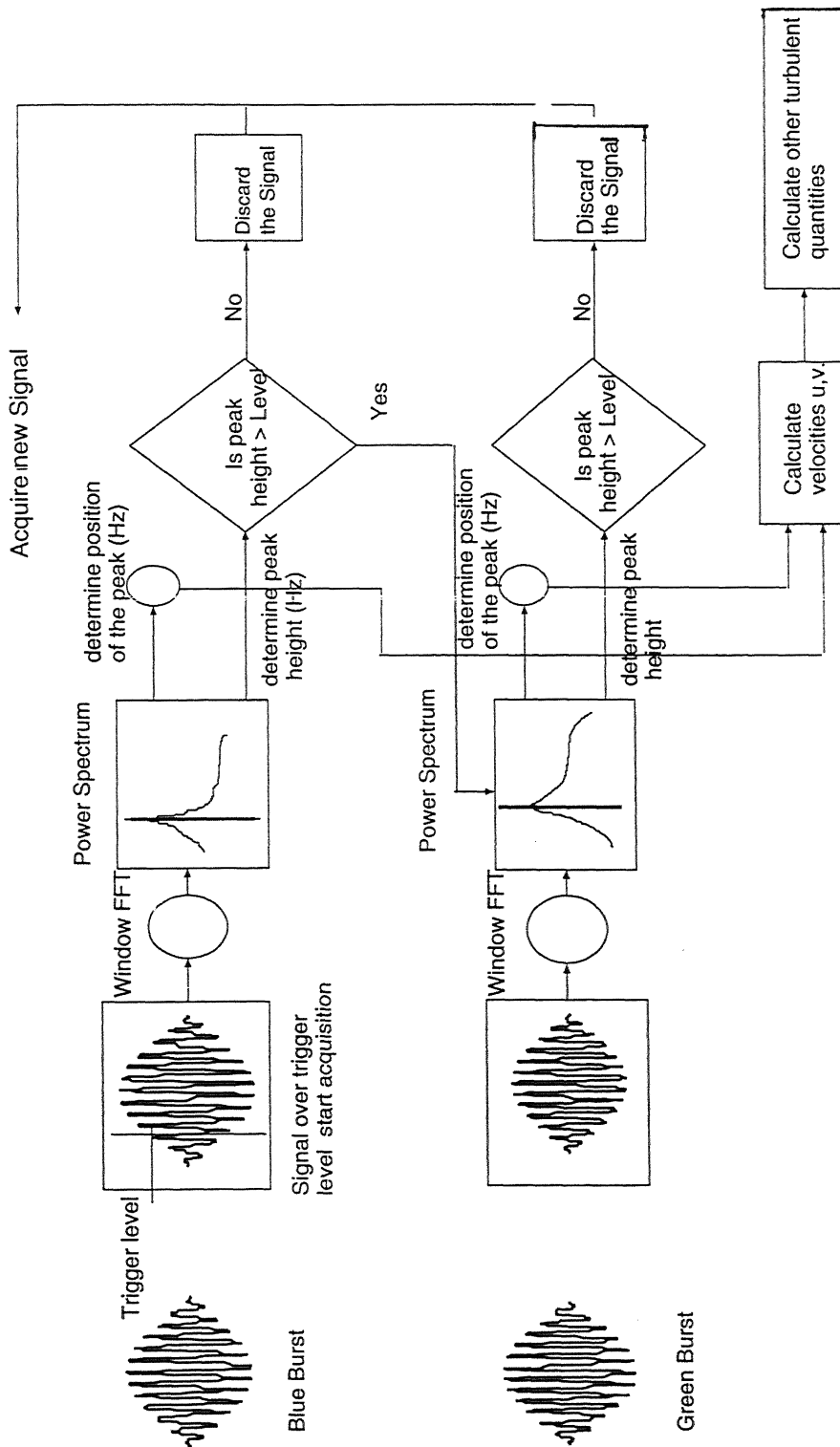
Fig.12   Digital Signal Processing inside the Computer

taken.

$$StatisticalError = \frac{\sigma}{\sqrt{n}}$$

We can reduce the statistical error by increasing the number of observations taken. But there is limit to that route as a large number of observations means a longer measurement time. The total estimated error in our measurements i.e. the error in the the values of $\overline{u}, \overline{v}, \overline{u'}^2, \overline{v'}^2, \overline{u'v'}$ is $\approx 5\%$ of u_{ref}.

Chapter 3

Description of Flow

3.1 Cylinder Without a Free End

Consider the pressure distribution on an infinite cylinder as shown in Fig. 13. The solid line in the Figure shows the pressure distribution as predicted by the potential flow theory. However, due to viscous effects, the boundary layer detaches itself from the wall close to $\theta = 90$ degrees, and the pressure in the wake remains close to the separation-point pressure. The actual pressure distribution is shown by the dotted line in Fig. 13. Now since the wake pressure is less than the pressure in the forward region of the cylinder, it experiences a drag force in the flow direction. This type of drag is called pressure drag or form drag.

Coefficient of lift and drag, base pressure (i.e. pressure at a point which is 180 degrees from the front stagnaton point), and separation points for a flow over an infinite cylinder have been investigated widely by the researchers. With a decrease in the base pressure, the recirculation region becomes prominent. Instabilites are created in the recirculation region from the downstream end of the separation bubble. As the Reynolds number increases the amplitude of maximum wake -velocity fluctuations increases. With an increase in the wake instability, the velocity fluctuations increase thereby lowering the base pressure. With increasing oscillations the separation bubbles detach and bring about a dramatic change in the flow structure.
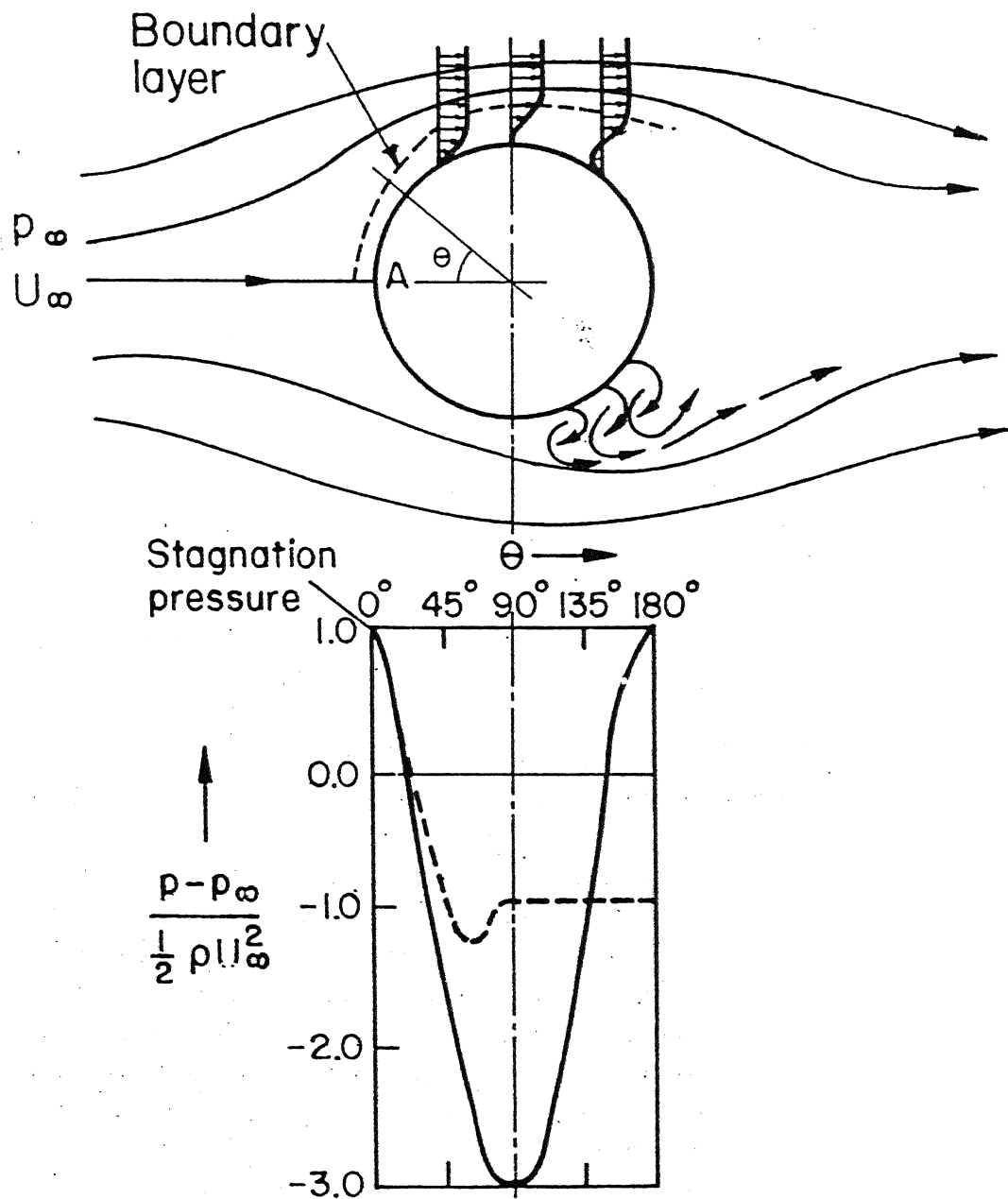
26

Fig.13　Boundary Layer Separation and pressure distribution on a long cylinder[14]

3.1.1 Wake Structure as a function of Reynolds Number

Morkovin (1964) has explained the wake structure for flow across an infinite cylinder as a function of Reynolds number. At very low Reynolds number (≤ 1) the flow smoothly divides and reunites around the cylinder (Fig. 14a). At a Reynolds number of about 4, flow separation occurs and two symmetrical standing eddies are formed. These eddies, also called separation bubbles remain steady but grow in size up to a Reynolds number of about 40 (Fig. 14b).

When the Reynolds number reaches nearly 40, the eddies begin to oscillate with time and an asymmetry is created in the wake. As the Reynolds number increases above 90, the eddies are shed alternately from the top and bottom of the cylinder. This regular pattern of alternately shed clockwise and counterclockwise vortices form a von Karman vortex street (Fig. 14d). The vortex-shedding phenomenon creates a periodicity in the flow field which is charaterized by the vortex-shedding frequency. The non-dimensional vortex- shedding frequency is known as Strouhal number.

As the Reynolds number is further increased to about 500, multiple frequencies of vortex shedding appear and the wake tends to become turbulent. The structure of a turbulent wake is strikingly different from the ones at low Reynolds numbers (See Figs. 14e and 14f).

3.2 Cylinder with a Free End

For a cylinder with a free end, the flow consists of three prominent regions. The first is the flow over the cylinder top, then there is the middle region and lastly, the region containing the cylinder base. The main flow, as it approaches the cylinder, gets displaced towards the body junction. This is due to the distribution of total pressure in the boundary layer.

In the front of the cylinder, as the flow proceeds towards the free end, sepa-

$$Re = U_\infty D / \nu$$

Re ~ 1

(a)

3 < Re < 40

(b) Twin-vortex stage

U

(c) Incipient Karman range

90 < Re < 500

(d) Pure Karman range

500 < Re < 2 × 10⁵ Turbulent wake

(e) Laminar boundary layer

Re > 2 × 10⁵

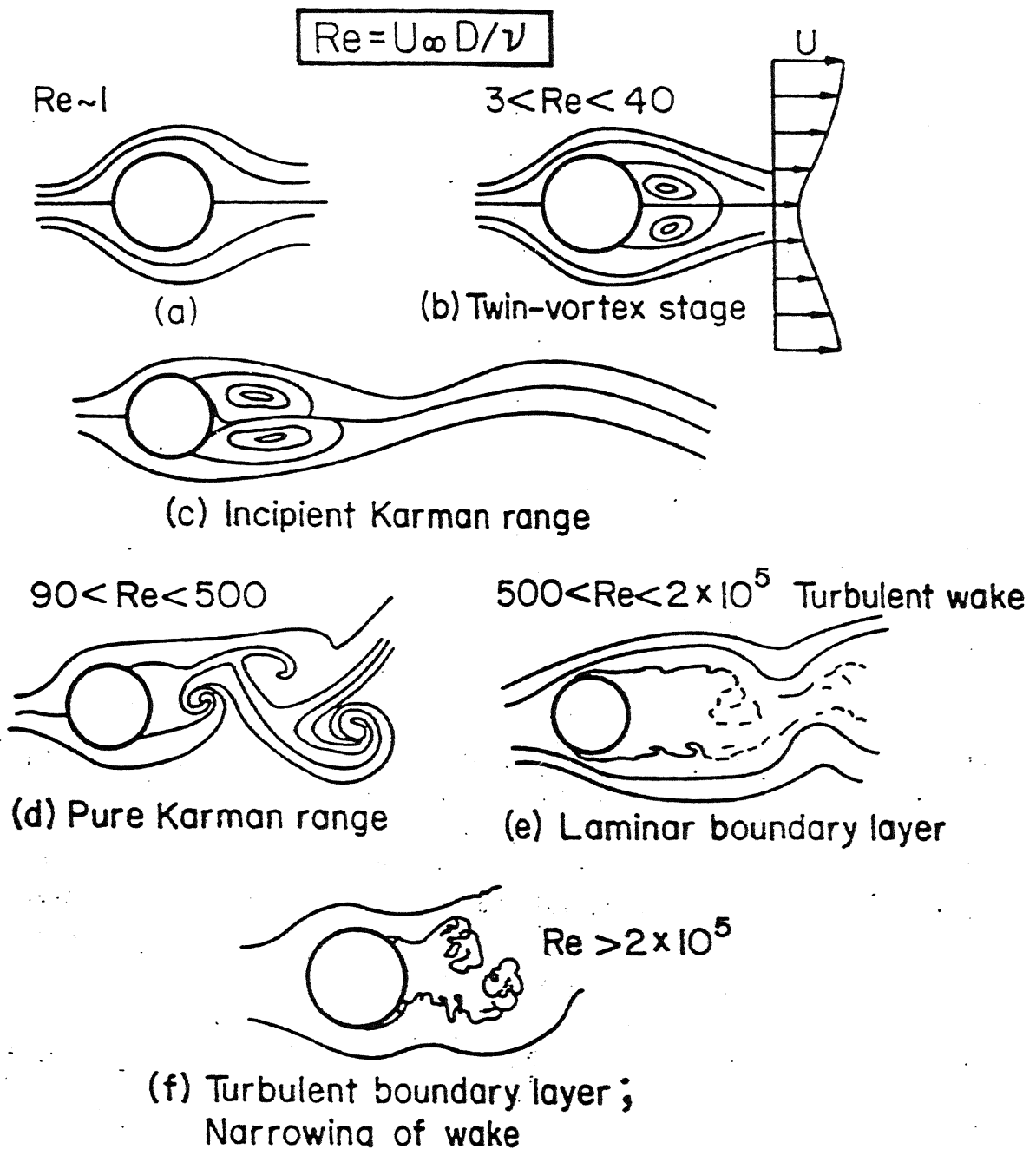(f) Turbulent boundary layer;
Narrowing of wake

Fig.14   Wake Structure as a function of Reynolds Number for a Long
Cylinder[14]

ration occurs at the leading edge. The result is a sickle shaped flow region with a predominant lateral flow component (Fig. 15e). Two vortices with opposite sign are observed (Fig. 15b). Because of the oncoming turbulent shear flow, momentum transfer takes place and the separated flow is forced to reattach at the cylinder top. The material outside the leading edge separation region and outside of the reverse flow region, is carried along by the lateral flow around the cylinder tip.

If we view the flow from the side we notice that upto an angle of 60 degrees, an upward flow occurs (Fig. 15c). A part of this flow gets separated at the cylinder edge . Other streamlines move up and down without reaching the top. We can see a complex vortex structure which is having a horizontal axis. Two flow regions are visible, one is having a reverse flow while the other region exhibits streamlines which proceed inclined upward. The effect of these vortices is that they delay the flow separation in the tip region as compared to the middle region of the cylinder. The separation at the tip region occurs at nearly 150 degrees.

In the base region a horseshoe vortex exists. It wraps itself around the body and trails downstream. The wake in this region consists of two vortices with vertical axis. A part of the horseshoe vortex turns into these vertical eddies. Nearly half a diameter behind the cylinder, the flow direction turns forward.
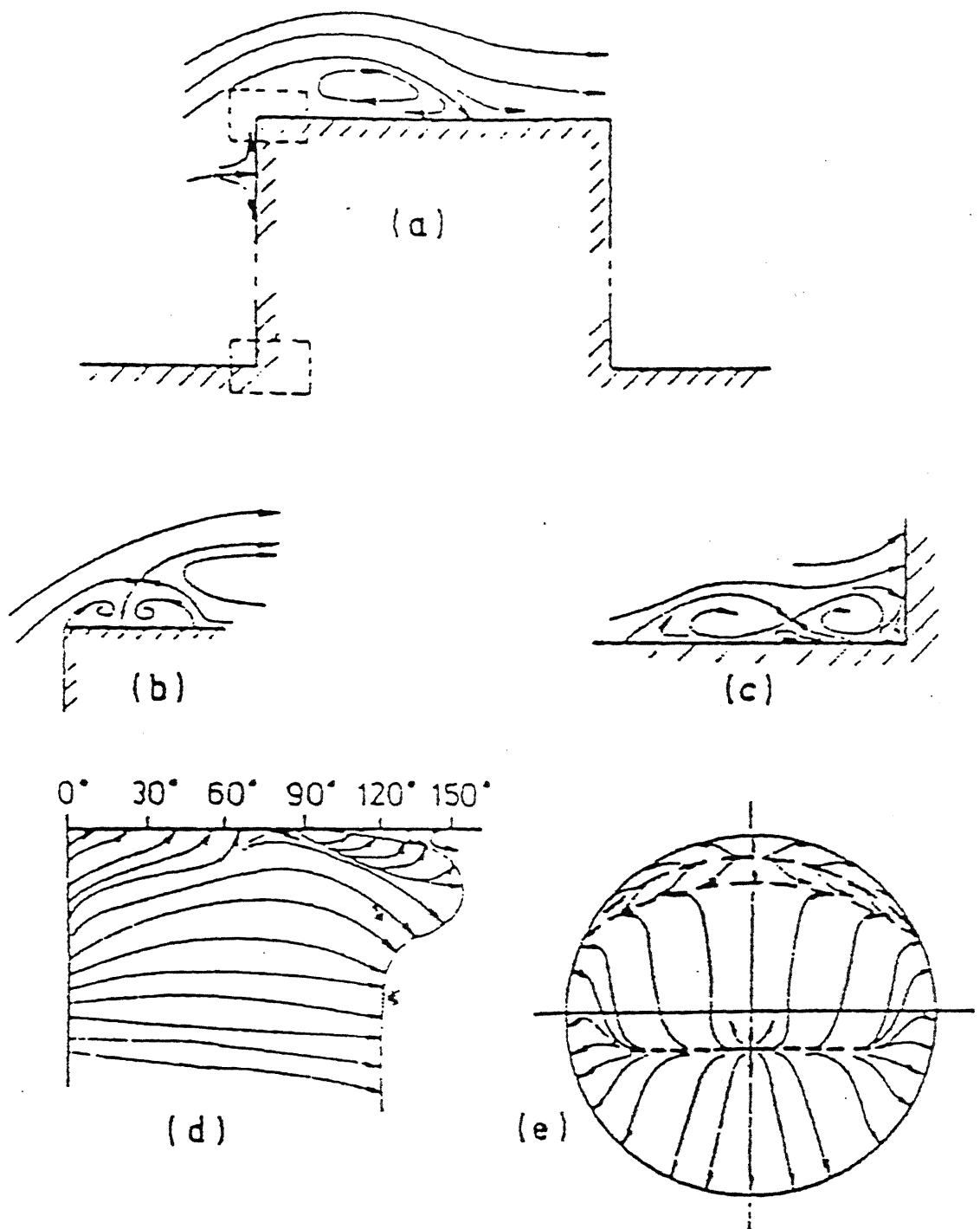
Fig.15　Description of Flow across a Finite Height Circular Cylinder[10]

Chapter 4

Results and Discussion

The contours of time mean velocities $(\overline{u},\overline{v})$, the turbulent stresses $(\overline{u'^2}, \overline{v'^2}, \overline{u'v'})$ and the vector plots for the long cylinder as well as the finite cylinder will be presented here. The contour plots have been interpreted and detailed comparisions have been made between finite and infinite cylinder results. Several contrasting differences are brought out in the contour profiles of both cases which help us understand the flow-structures better. Measurements were made in one half of the flow region, assuming symmetry of the flow about the cylinder center-line. However just to confirm the symmetric nature of flow, one extra row of points was added to the measurement region in the other half. The annular region between the hexagon and the cylinder is the one in which measurements could not be taken. The reason was the obstruction of the interfering beams by the cylinder making measurements impossible in the vicinity.

4.1   Longitudinal time-mean velocity $(\overline{u})$

Figure 16 shows the contour plot for the longitudinal mean velocity $(\overline{u})$ for the long cylinder. The recirculation region is found to be approximately $0.8D$. Refer to Fig.22 which shows the $\overline{u}$ contours for the finite cylinder at the free end. The recirculation region in this case is greatly reduced. It is confined within $x = 0.25D$. The zero mean velocity line is not visible in the plot as measurements

could not be taken very close to the cylinder. The recirculation region for the finite cylinder at the plane $z = -1D$ (Fig.28) appears to be lengthened considerably. The recirculation region in this case measures approximately $1.2D$ as compared to $0.8D$ for the long cylinder. Beyond the recirculation region, the finite cylinder shows a faster approach to the free-stream velocity when compared with the long cylinder. Comparision of the $\overline{u}$ contour plots for the finite cylinder (Figures 22 and 28) reveals that the approach to the free-stream velocity is much faster at the free end than at $z = -1D$.

4.2   Transverse time-mean velocity $(\overline{v})$

Figure 17 shows the contour plot of the lateral mean-velocity $(\overline{v})$ for the long cylinder. The profile is almost antisymmetric except that the zero v-velocity line does not lie perfectly on the center-line of the cylinder. The maximum value of transverse mean-velocity in the wake occurs at about $x = 1.3D$. Figure 23 shows that the free end of the finite cylinder exhibits almost perfect antisymmetry in the $\overline{v}$ contours. The maximum of the v-velocity is almost at the same x location as the long cylinder. Figure 29 shows the contours for the $z = -1D$ plane. The maximum of the v-velocity in the wake seems to be shifted downstream and occurs at about $x = 2D$.

4.3   Turbulent normal-stress in the streamwise direction $(\overline{u'^2})$

For the long cylinder the contours of streamwise fluctuations appears to be quite antisymmetric (See Fig.18). The maximum of $\overline{u'^2}$ fluctuations occur at approximately $x = 1D$. Figure 24 shows the $\overline{u'^2}$ contours for the free end of the finite cylinder. An antisymmetric pattern is exhibited but the level of fluctuations is considerably lower as compared to the long cylinder. The maximum of $\overline{u'^2}$ lies at about $x = 0.75D$. Consider the $\overline{u'^2}$ contours for the $z = -1D$ plane of the finite

cylinder as shown in Fig.30. The level of fluctuations though is somewhat higher than that at the free end but is significantly lower than in the long cylinder case. The $\overline{u'^2}$ contour plot exhibits a maximum at $x = 1.75D$. Comparision of the $\overline{u'^2}$ contours for the two planes of the finite cylinder reveals that the point of maximum fluctuation level shifts downstream as we move from the free end towards the base region. In other words the region in which the effects of turbulence are felt tends to become larger as we move towards the base of the finite cylinder. This observation can however be stated more confidently only after having more observation planes in the base region of the finite cylinder.

The long cylinder exhibits a higher level of streamwise velocity fluctuations compared to the finite cylinder. Also the region in which the fluctuation levels are significant is much longer and wider for the long cylinder.

The turbulence region for the free end of the finite cylinder is greatly minimized and is confined within $x = 1.5D$. Another inference which can be drawn out from these plots, is that the turbulence increases as we move away from the free end of the finite cylinder towards its base.

4.4 Turbulent normal stress in the transverse direction $\left(\overline{v'^2}\right)$

The transverse velocity fluctuations $\overline{v'^2}$ for the long cylinder (Fig.19) appear to be reasonably symmetric when compared with those of the finite cylinder (Figures 25 and 31). The maximum of $\overline{v'^2}$ for the long cylinder occurs at $x = 1.4D$ and lies at the centerline of the cylinder. This is far downstream when compared to the location of the maximum, of $\overline{u'^2}$ for the long cylinder ($x = 1D$). Also we note that the level of the transverse fluctuations $\overline{v'^2}$ is significantly higher than that of the longitudinal fluctuations $\overline{u'^2}$ for the long cylinder.

For the free end of the finite cylinder the level of v-fluctuations is slightly lower as compared to the u-fluctuations. At $z = -1D$ location for the finite cylinder,

the v-fluctuations are higher than the u-fluctuations, though the difference is not so pronounced as in the case of the long cylinder. The maximum of $\overline{v'^2}$ for the $z = -1D$ plane of the finite cylinder lies at $x = 2D$. Same observations as were made for the $\overline{u'^2}$ contours are made here again. The v-fluctuations occuring in the wake of the long cylinder are significantly greater than those in the case of the finite cylinder. The free end of the finite cylinder exhibits the minimum level of transverse fluctuations. Also the fluctuations die out quickly with x at the free end. The region of turbulent fluctuations is the largest in the case of the long cylinder.

4.5   Turbulent shear stress $(\overline{u'v'})$

The $\overline{u'v'}$ contours for a long cylinder (Fig.20) exhibit an antisymmetric pattern. The maximum value of the turbulent shear stress occurs at $x = 1.4D$. The turbulent shear stress pattern of a finite cylinder at the free end hardly shows any variation. Only the zero shear stress line is visible in the contour plot (Fig.26). This means that the region in which turbulent shear stress values are considerable is a very small area in the near wake of the cylinder. It occurs that the three dimensional nature of flow occuring at the free end suppresses the turbulent shear stress. The $z = -1D$ plane of the finite cylinder also exhibits an antisymmetric behaviour (Fig.32). The level of turbulent shear stress is however much less than that of the long cylinder. The maximum of the shear stress profile is however shifted downstream and occurs at $x = 1.8D$. As compared to the long cylinder the region of prominent turbulent shear stress appears to be narrowed.

4.6   Velocity vector plots

The velocity vector plot for the long cylinder shows two symmetric recirculation vortices (Fig.21). The reattachment occurs at $x = 1.3D$. Comparing with the velocity vector plot for the free end of the finite cylinder (Fig.27) we note that the

recirculation region is greatly suppressed and separation bubbles are not observed. The complex three-dimensional flow structure at the free end of the finite cylinder tends to suppress the separation of the flow. The vector plot at $z = -1D$ plane of the finite cylinder (Fig.33) appears to be lengthened considerably, the separation region stretching upto $1.7D$. But the width of the separation region appears to be slightly less than the long cylinder. The smaller separation region at the free end signifies a delayed separation, as compared to the middle region of the finite cylinder. This observation is in agreement with the findings of Hölscher and Niemann (1987). In their study, they have reported the separation at the free end to occur at nearly 150 degrees, while outside the end region it occurs at about 120 degrees.
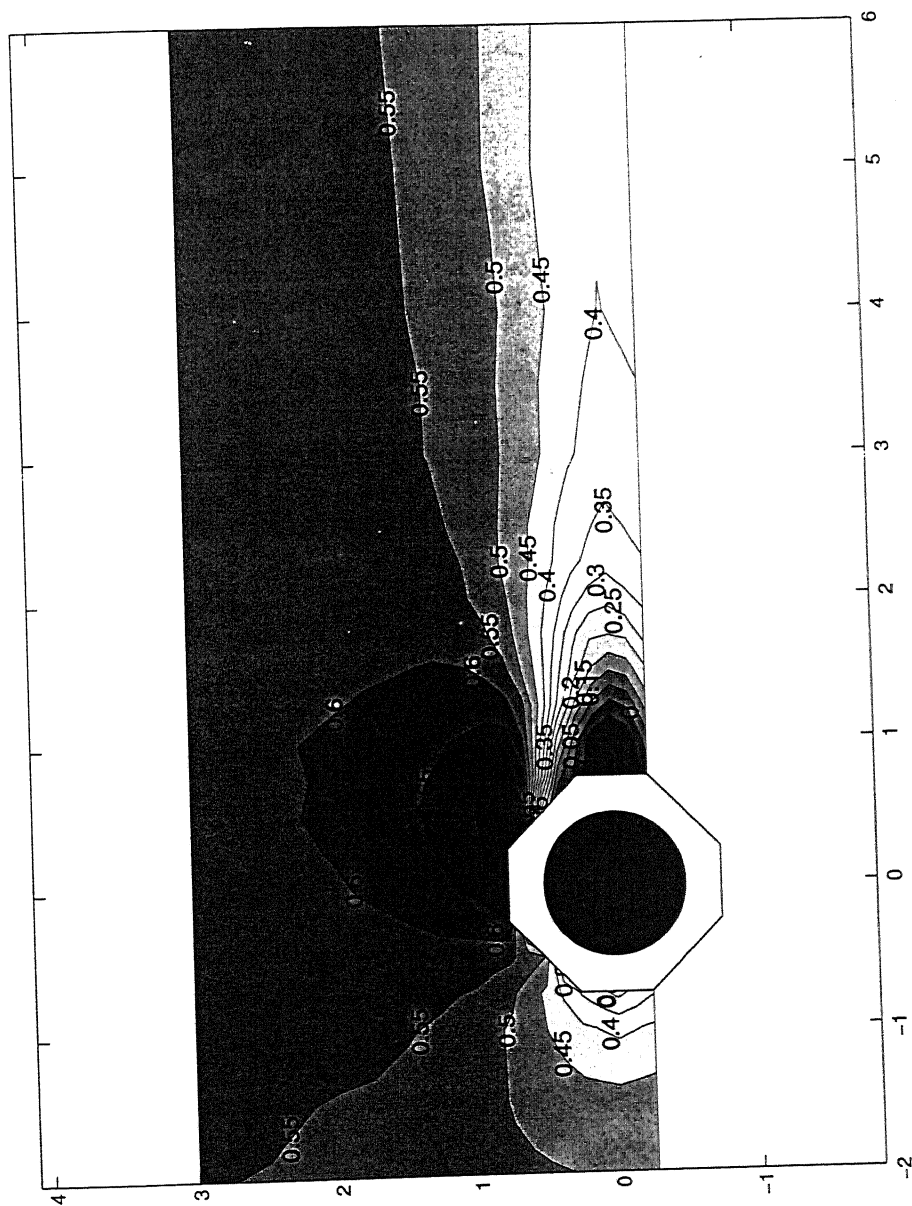
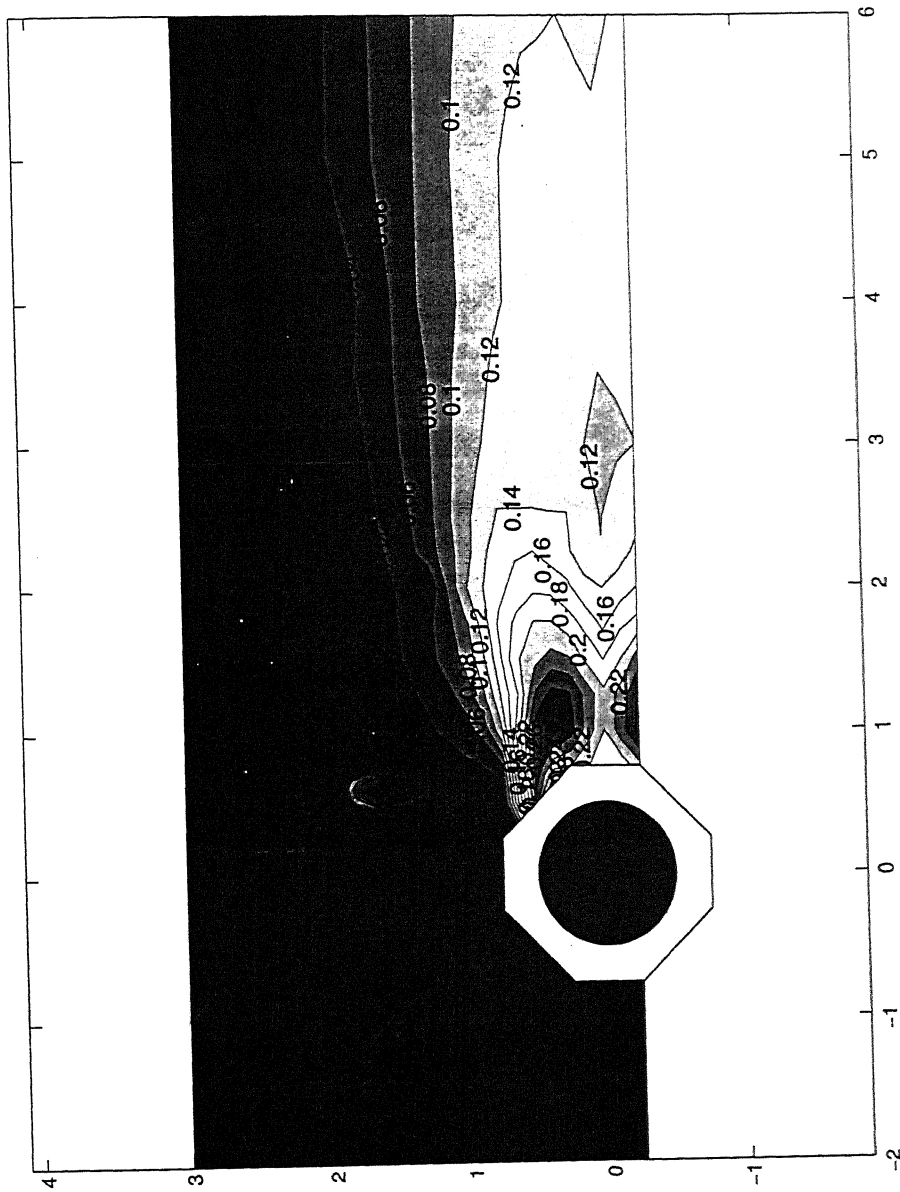Fig.16 Contours of time-mean u velocity ($\overline{u}$) for the long cylinder

Fig.17 Contours of time-mean v velocity $(\overline{v})$ for the long cylinder
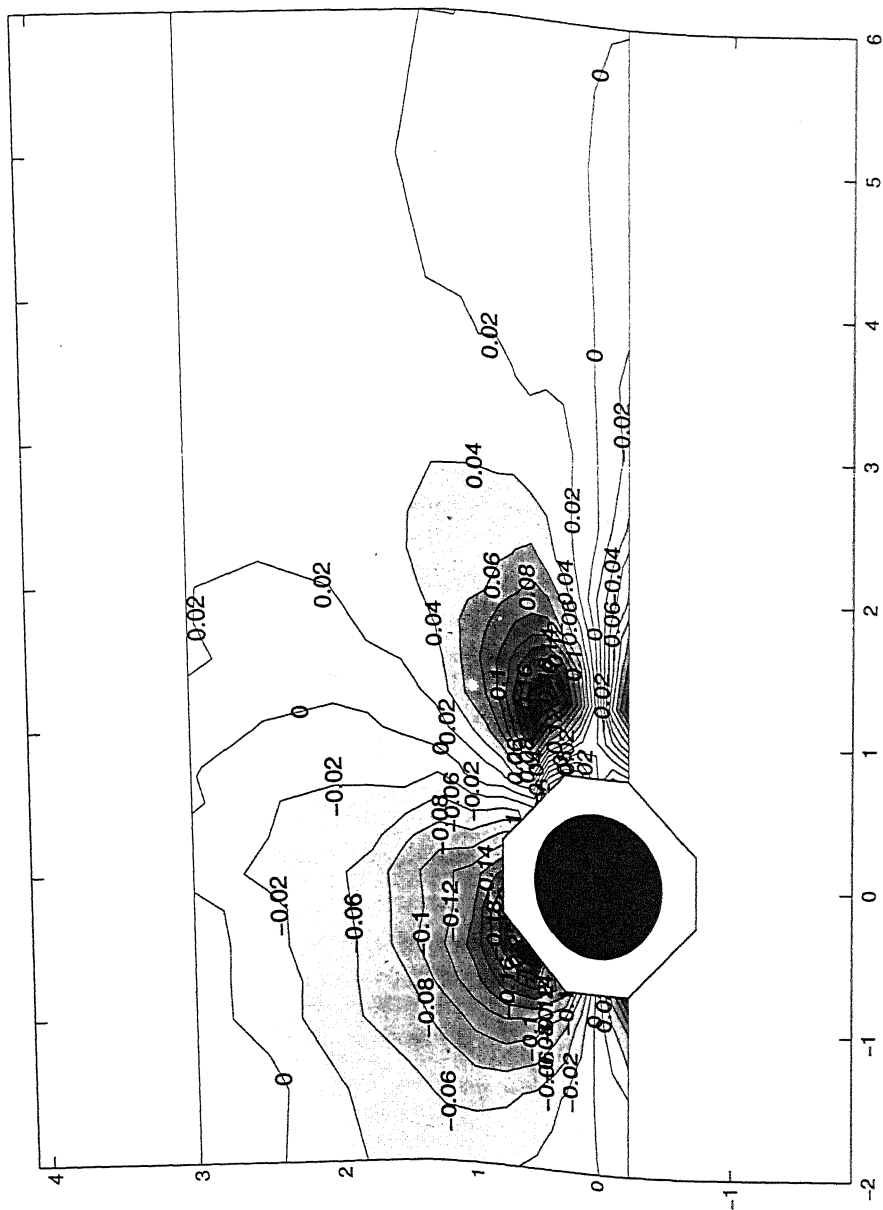
Fig.18　Contours of turbulent normal stress $(\overline{u'^2})$ for the long cylinder

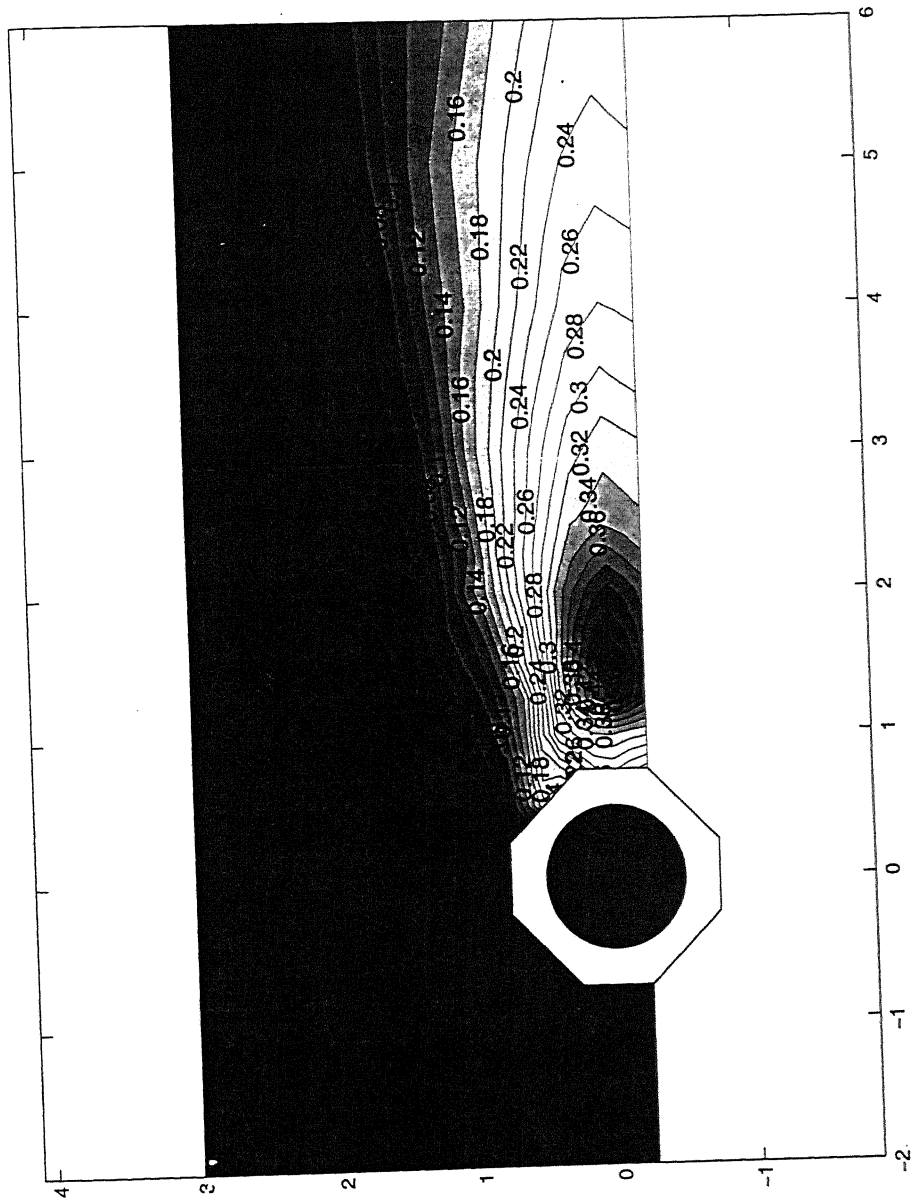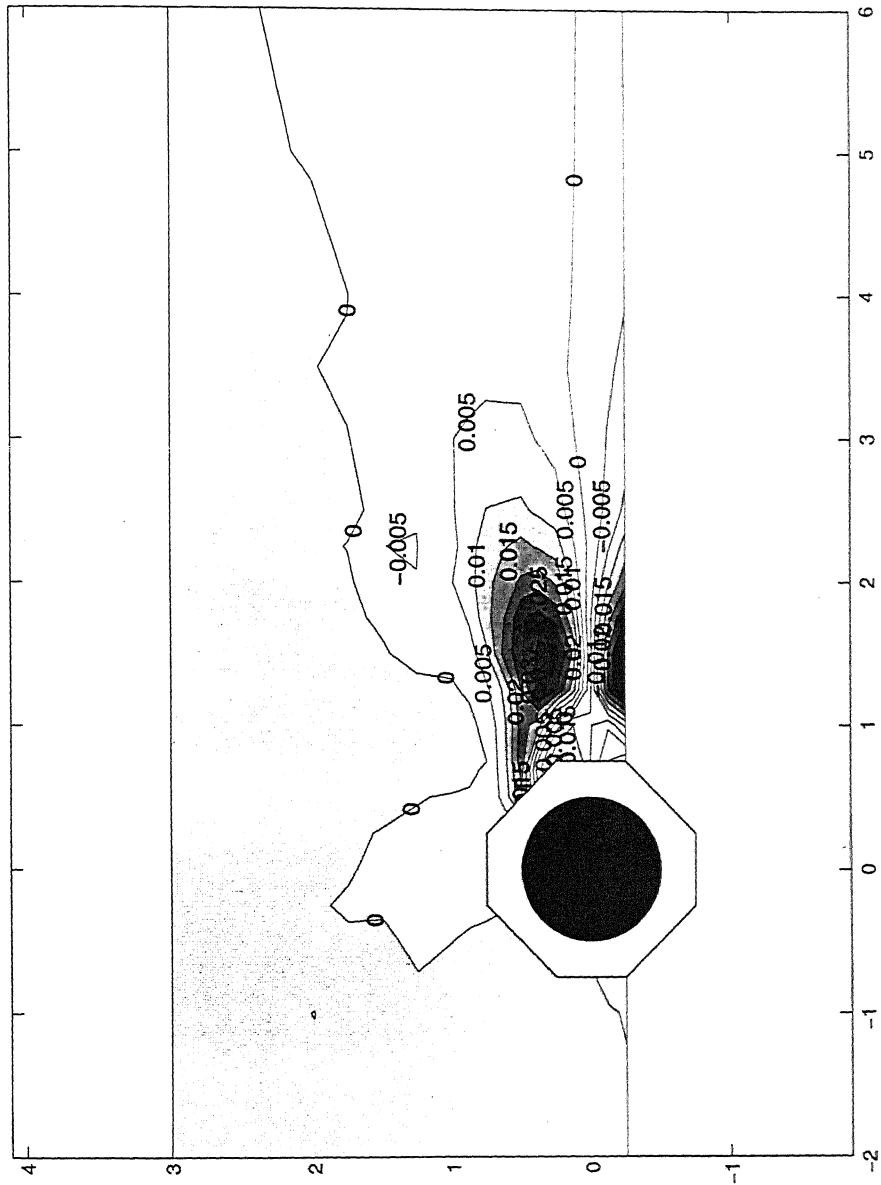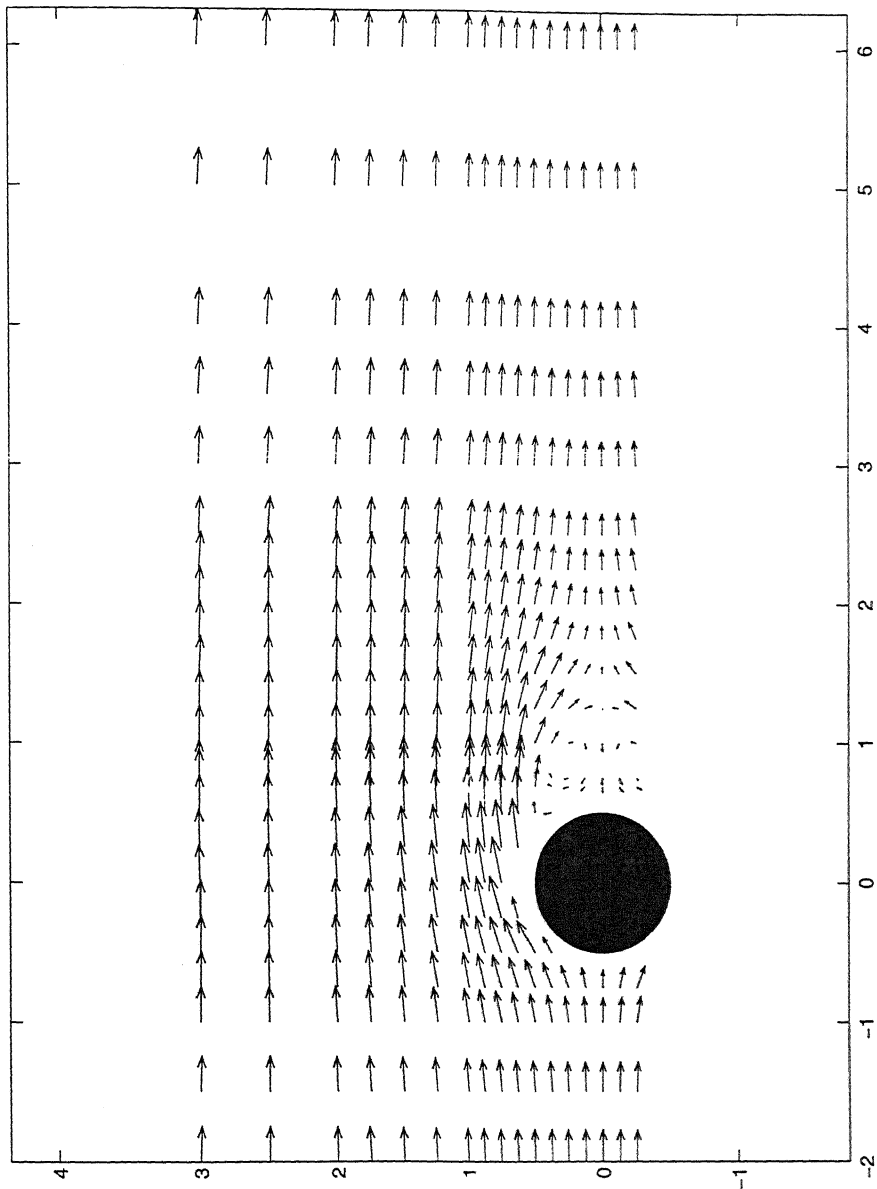Fig.19　Contours of turbulent normal stress $(\overline{v'^2})$ for the long cylinder

Fig.20　Contours of turbulent shear stress $(\overline{u'v'})$ for the long cylinder

Fig.21   Velocity vector plot for the long cylinder
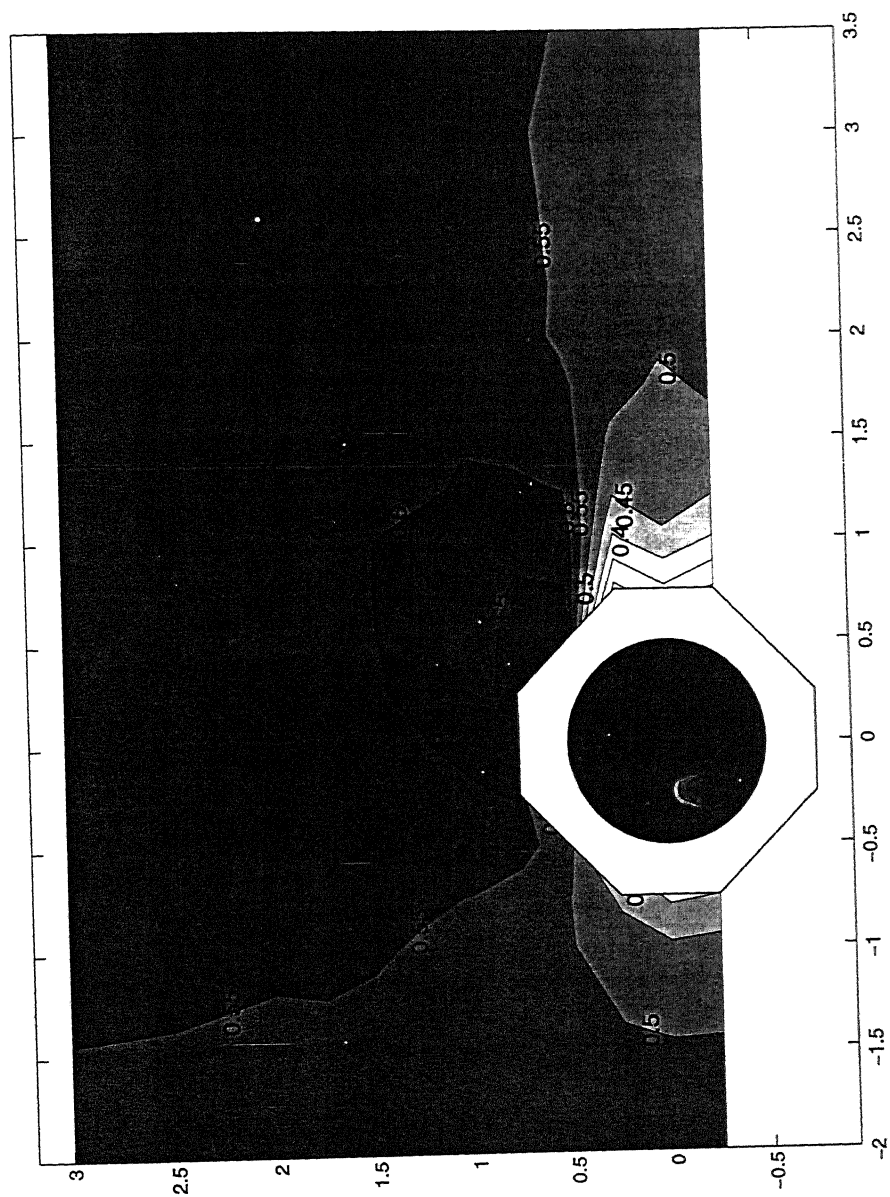
Fig.22　Contours of time-mean u velocity ($\overline{u}$) for the finite cylinder at $z = 0$
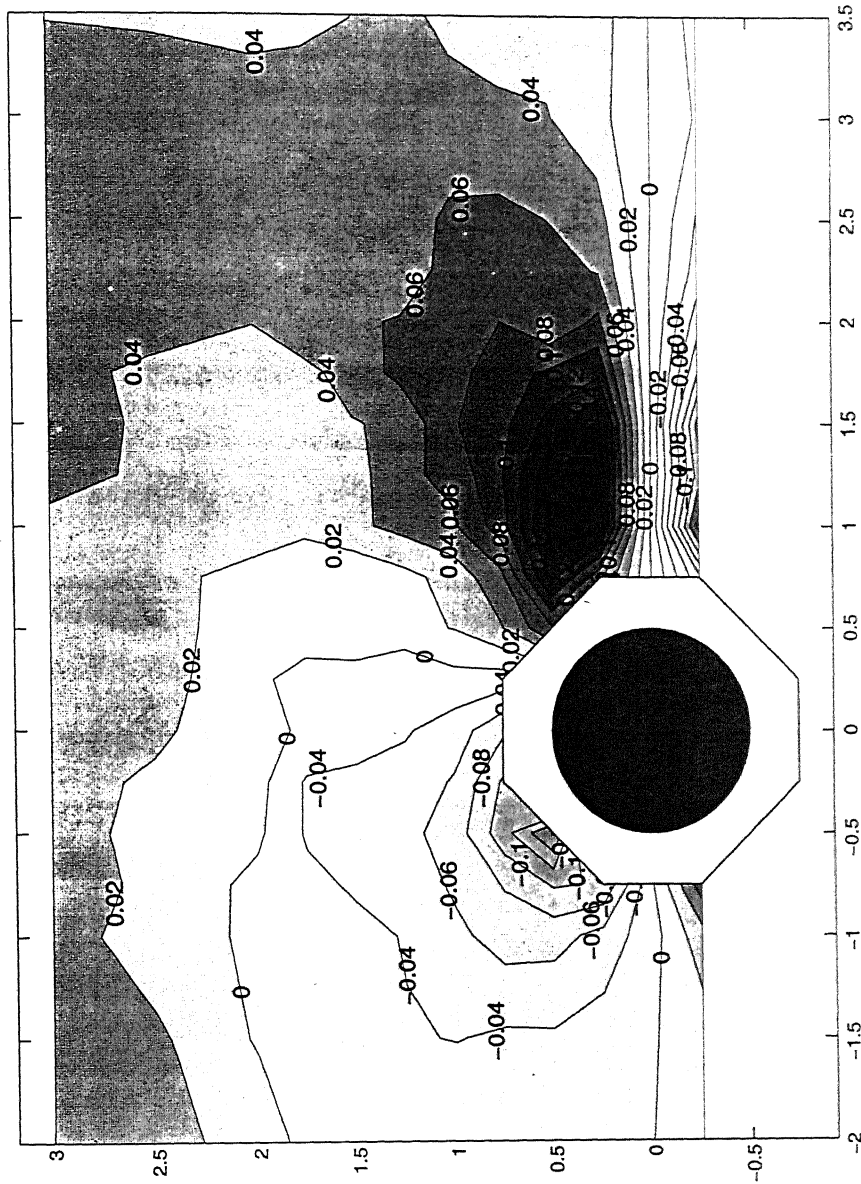(free end)

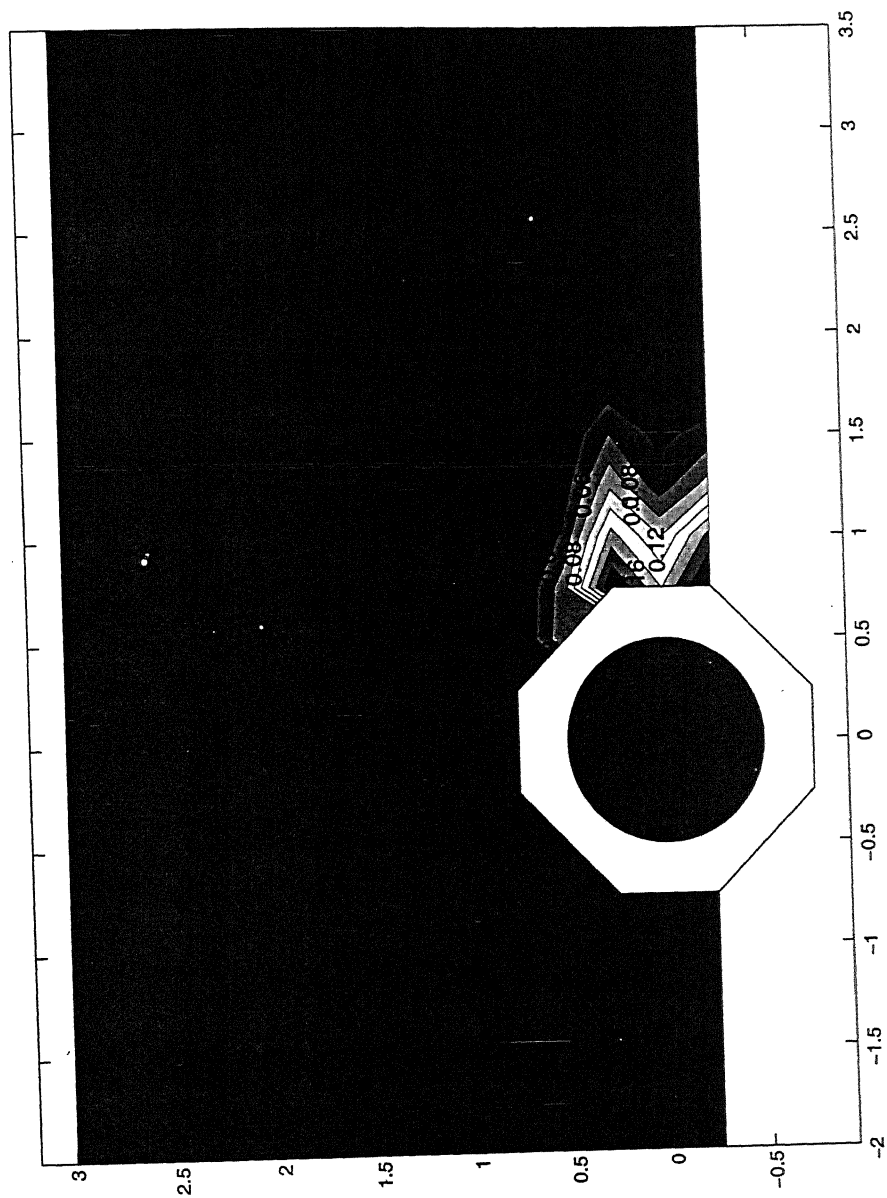Fig.23   Contours of time-mean v velocity ($\bar{v}$) for the finite cylinder at $z = 0$
(free end)

44

Fig.24   Contours of turbulent normal stress $(\overline{u'^2})$ for the finite cylinder at z=0
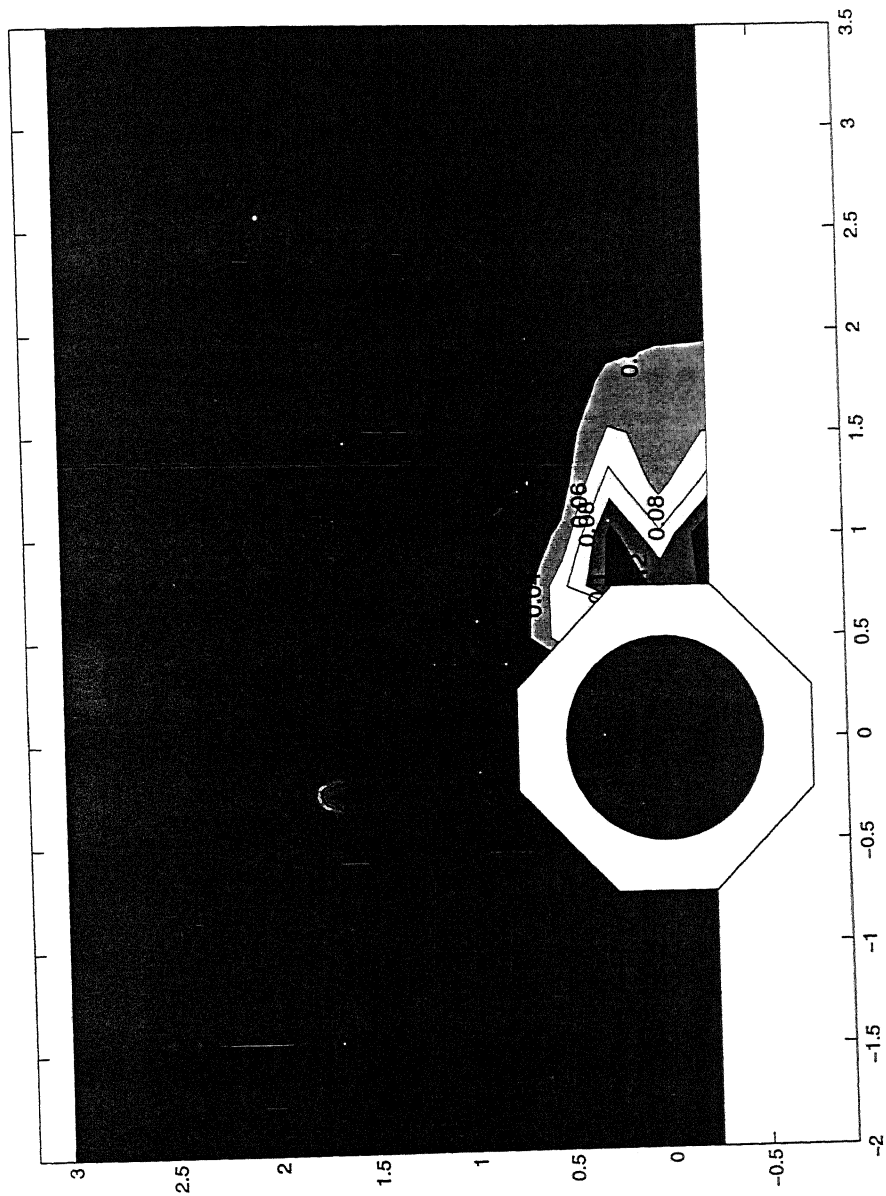(free end)

45

Fig.25　Contours of turbulent normal stress $\overline{(v'^2)}$ for the finite cylinder at $z = 0$ (free end)
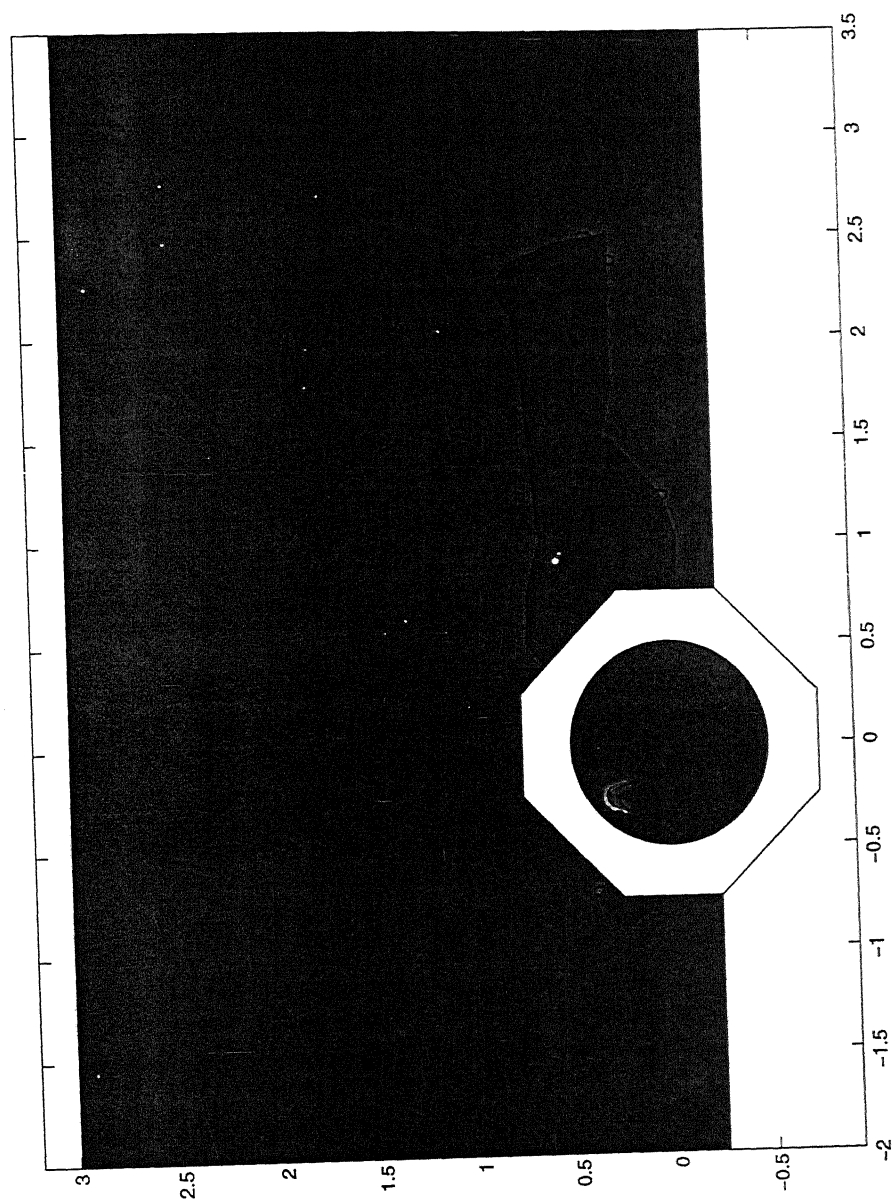
Fig.26 Contours of turbulent shear stress $(\overline{u'v'})$ for the finite cylinder at $z = 0$
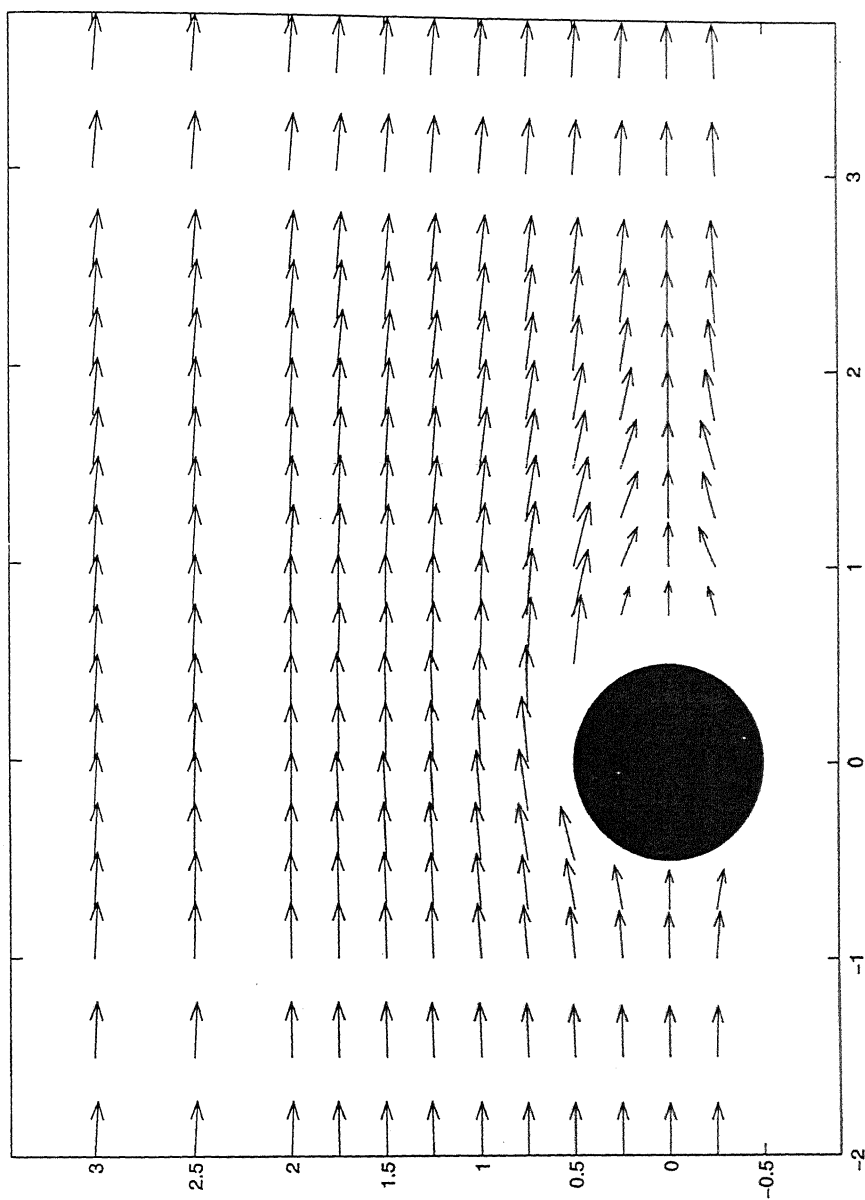(free end)

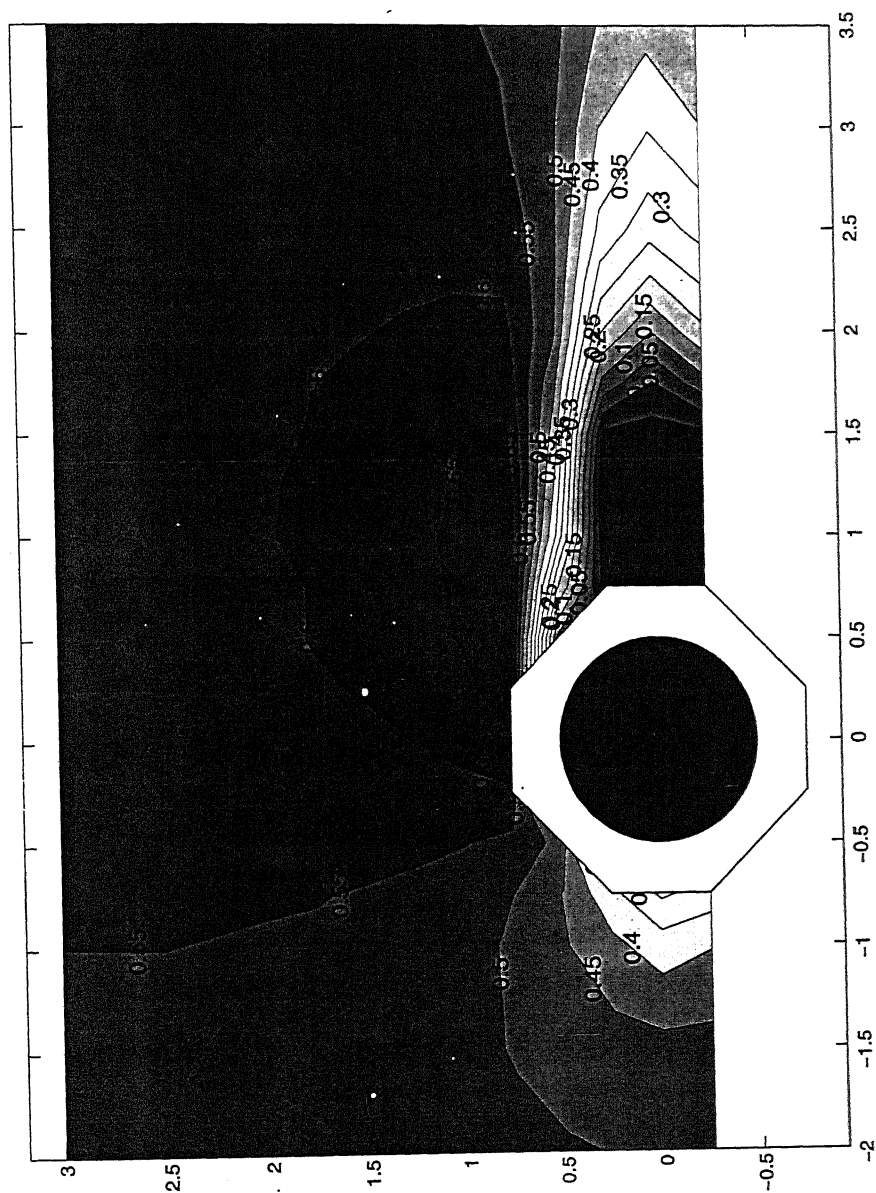Fig.27　Velocity vector plot for the finite cylinder at $z = 0$ (free end)

Fig.28　Contours of time-mean u velocity $(\overline{u})$ for the finite cylinder at $z = -1D$
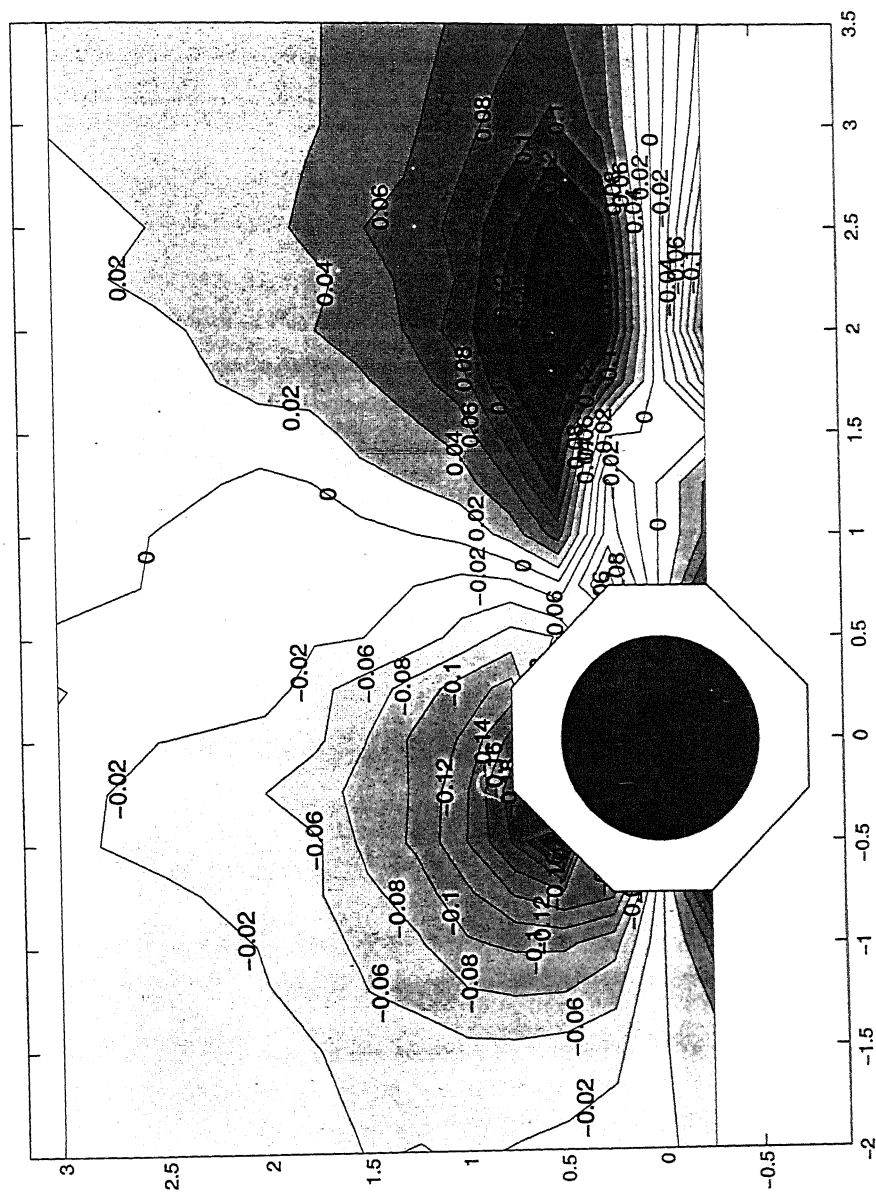
Fig.29   Contours of time-mean v velocity ($\overline{v}$) for the finite cylinder at $z = -1D$

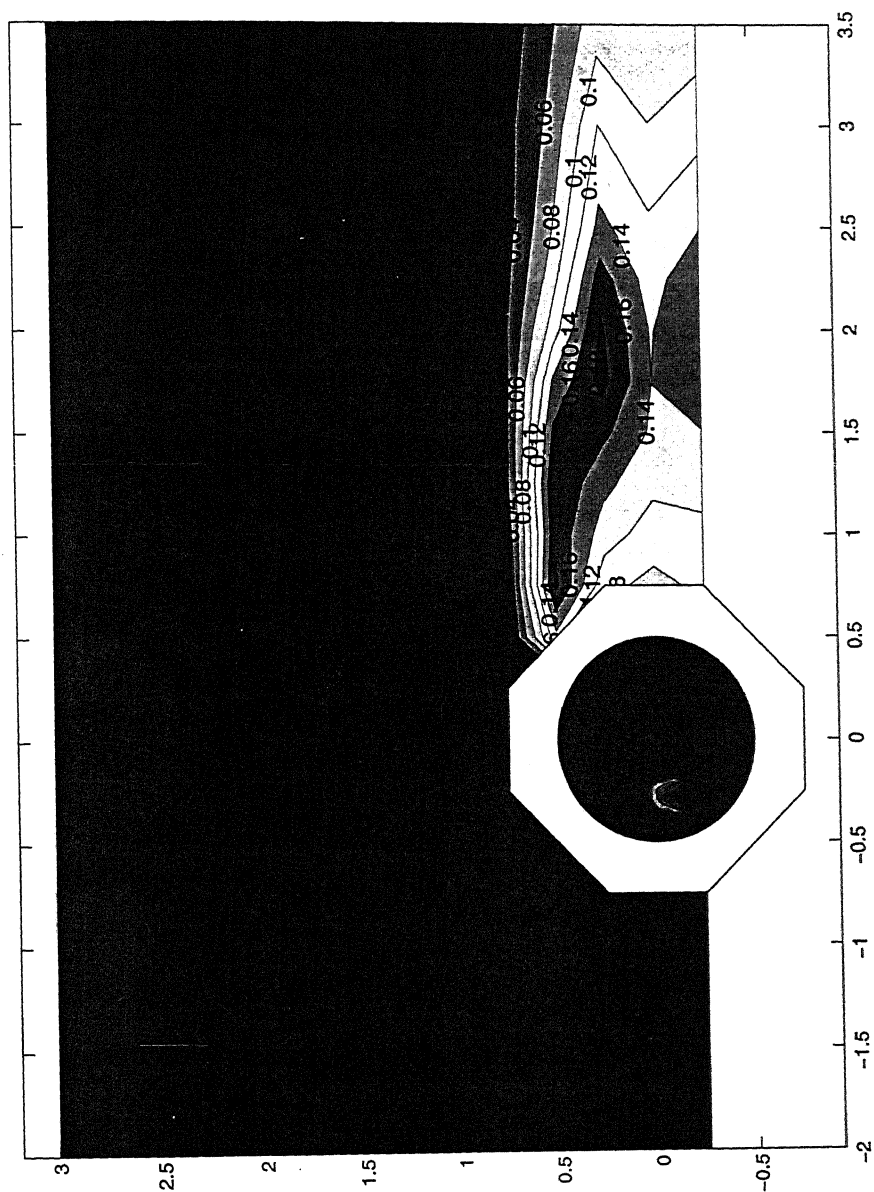Fig.30 Contours of turbulent normal stress $(\overline{u'^2})$ for the finite cylinder at $z = -1D$
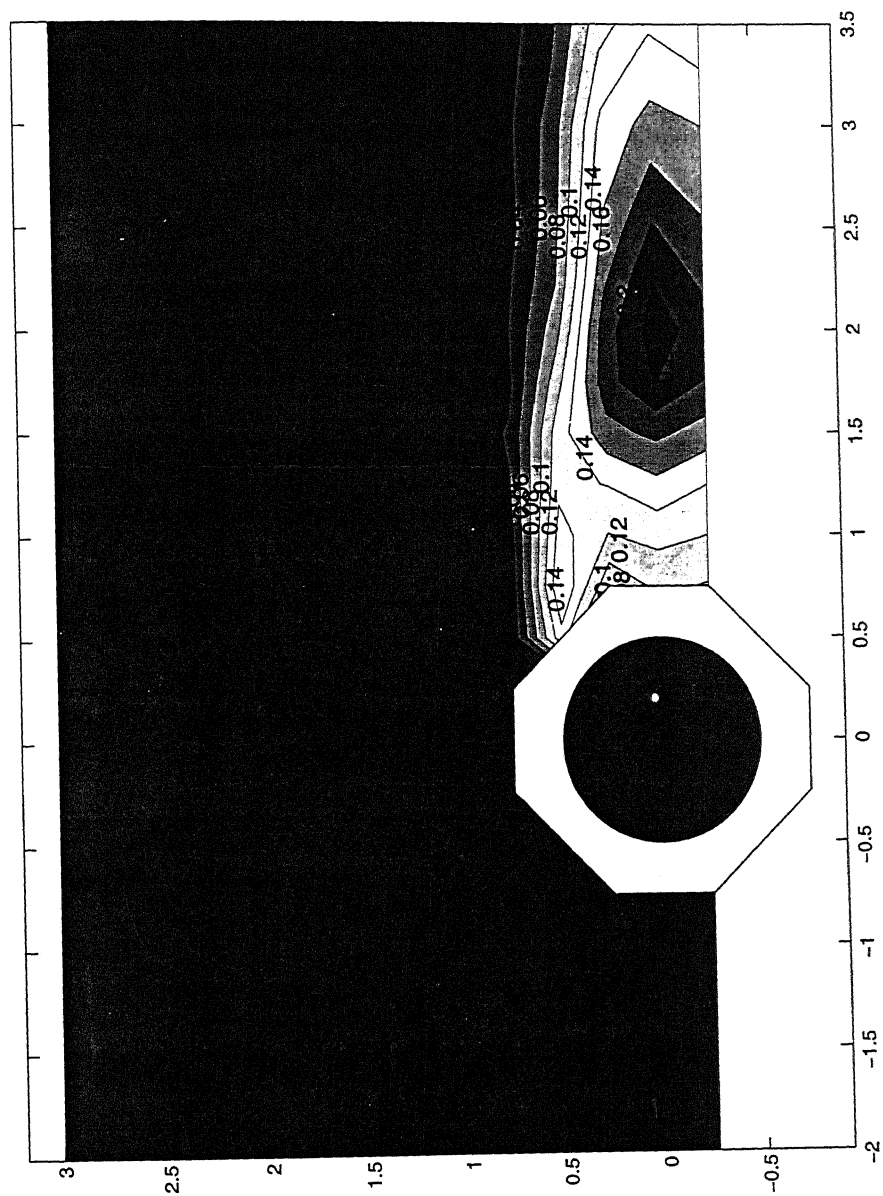
Fig.31　Contours of turbulent normal stress $(\overline{v'^2})$ for the finite cylinder at
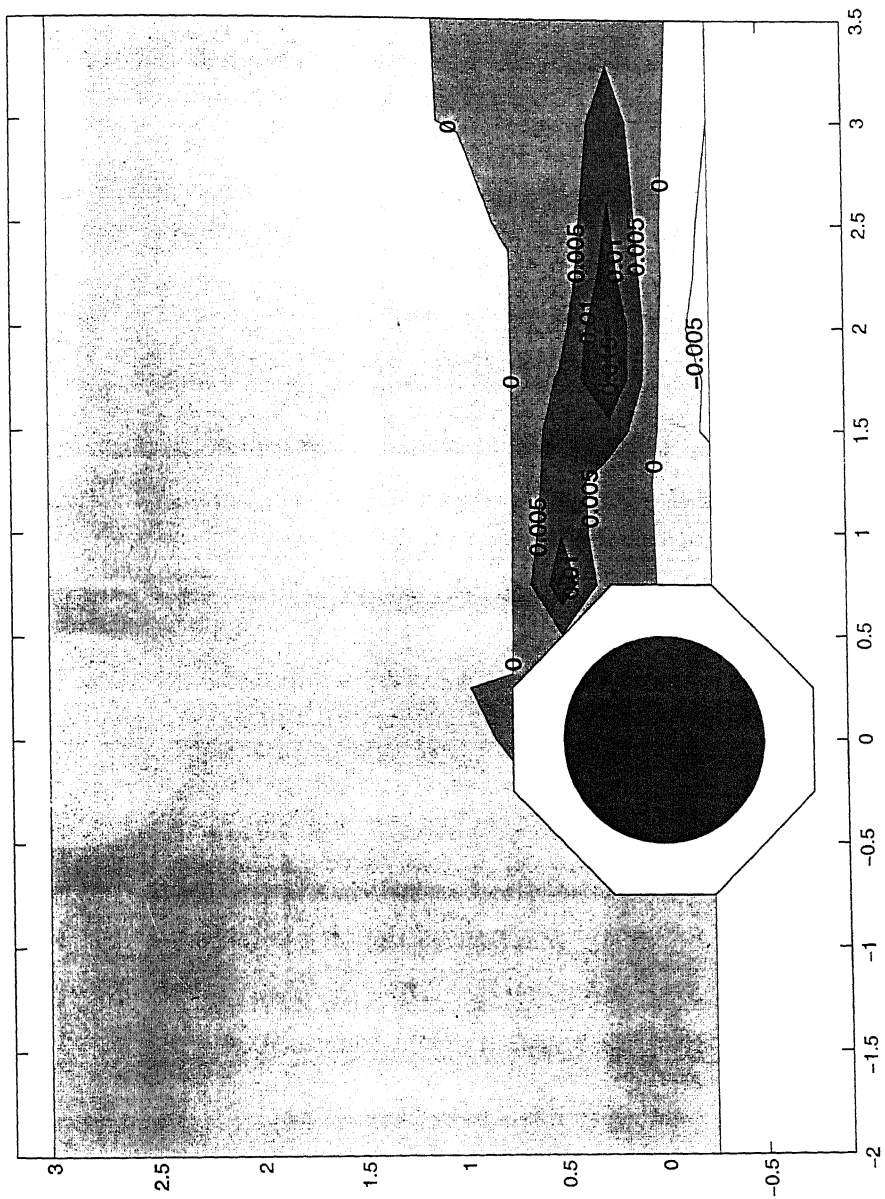$z = -1D$

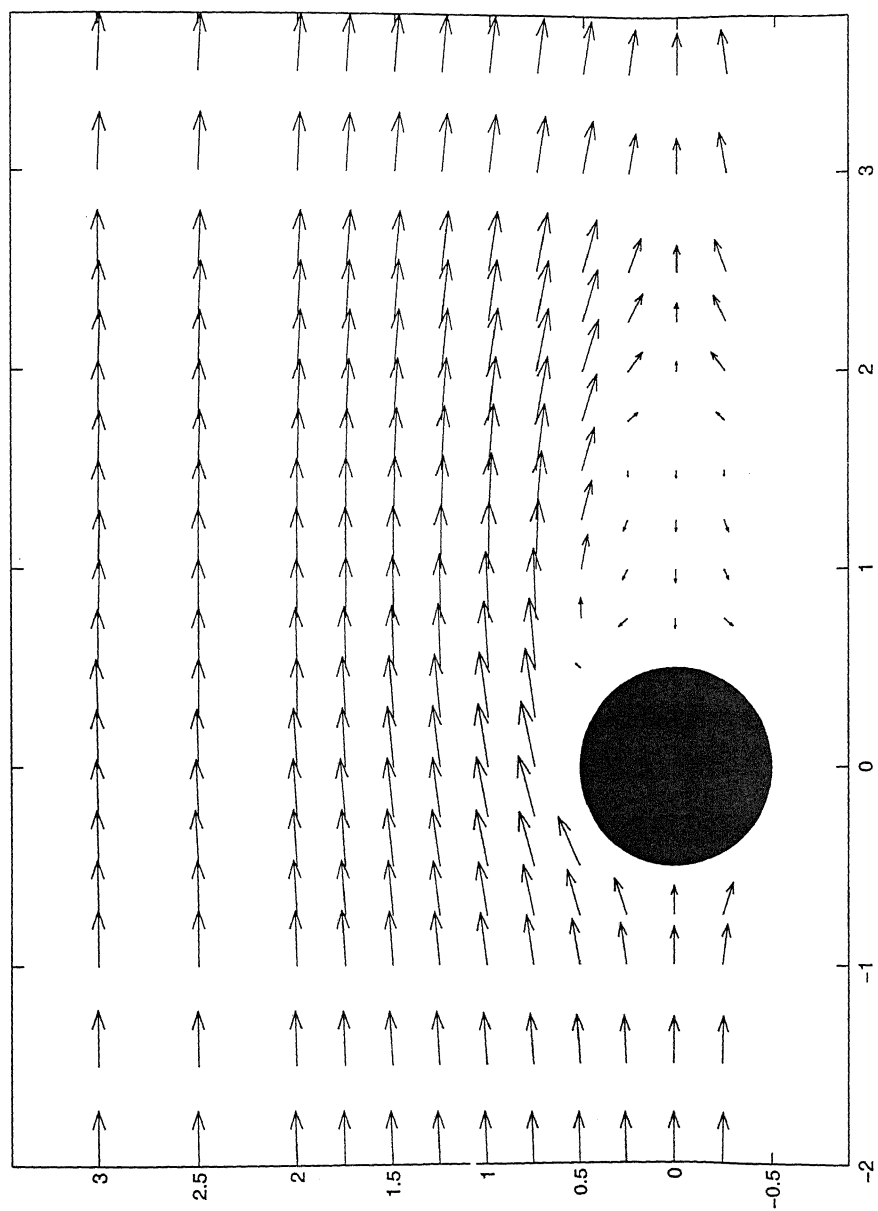Fig.32　Contours of turbulent shear stress $\overline{(u'v')}$ for the finite cylinder at $z = -1D$

Fig.33　Velocity vector plot for the finite cylinder at $z = -1D$

Chapter 5

Conclusions and Scope for Future Work

5.1 Conclusions

The wakes of a long circular cylinder and a finite circular cylinder have been studied experimentally. The Reynolds number for the investigation is 22000 and the l/d ratio of the finite cylinder is 5. The study is aimed at understanding the structure of the wake of the finite cylinder and contrast it with that of the long cylinder.

The contour plots for the longitudinal mean velocity $(\overline{u})$ for the finite cylinder reveal that the separation region is greatly suppressed at the free end when compared to the $z = -1D$ plane. The length of the separation zone observed at the free end is less than $0.25D$, while for the $z = -1D$ plane it is $1.2D$. From this, we infer that as we move away from the free end of the finite cylinder towards its base, the separation region becomes larger. Also the approach to free stream velocity is faster at the free end than in the middle region.

The turbulent u-fluctuations in the case of the free end of the finite cylinder are smaller in magnitude compared to the fluctuations in the $z = -1D$ plane. The turbulent u-fluctuations for the long cylinder are however larger in magnitude compared to the finite cylinder. Also the region of considerable turbulent u-fluctuations is smaller in the case of the finite cylinder. The free end of the

finite cylinder exhibits the lowest level of turbulent u-fluctuations. Similar observations can be made for the turbulent v-fluctuations and the turbulent shear stress profiles. All these observations lead us to the conclusion that for a finite cylinder the three-dimensional nature of the flow, due to the presence of the free end, suppresses turbulence in the wake. The most affected quantity being the turbulent shear stress. Moreover a reduction in the size of the zone, where the turbulent effects are significant, is also brought about.

The velocity vector plot shows that the separation is highly delayed in the case of the finite circular cylinder. Especially at the free end the recirculation region is confined to a very small area. The $z = -1D$ plane is close to the free end and the flow structure here is affected more by the flow in the tip region. At this plane also the phenomenon of delayed separation is evident, as the recirculation region is smaller as compared to the long cylinder. One thing which is evident is that as we go down towards the base of the cylinder the separation point moves forward.

5.2 Scope for Future Work

In the present work simple time-averaged quantities like $\bar{u}, \bar{v}, \overline{u'^2}, \overline{v'^2}, \overline{u'v'}$ and the velocity vector plots shave been analysed. The present finite cylinder data is inadequate to understand in detail the entire flow structure around the cylinder. The flow across a finite cylinder consists of three prominent regions: the tip region, the middle region and the base region. The present experiments are confined to the tip and the middle regions only, as data has been acquired for two planes: one containing the free end and the other one at $z = -1D$. In order to effectively cover all the three regions of flow, we need to acquire the data for at least $4-5$ planes, spanning the entire length of the cylinder. The base region which is dominated by a horse-shoe vortex structure, also needs to be investigated thoroughly as it significantly alters the flow structure by broadening the Vortex Street.

Besides the experiments, flow visualisation studies can also be carried out

to supplememt the experimental data. Flow visualisation helps us to identify different structures and patterns in the flow. Moreover the effect of different aspect ratios on the flow can also be studied. It would be an interesting exercise to see the effect of the aspect ratio on the vortex shedding pattern behind a cylinder.

Bibliography

[1] Achenbach, E., 1968, Distribution of local pressure and skin friction around a circular cylinder in a cross-flow up to Re=5.1**6, J. Fluid Mech., Vol. 34, pp. 625-640.

[2] Bearman, P.W. and Graham, J.M.R., 1980, Vortex shedding from bluff bodies in oscillatory flow: A report on Euromech 119. J Fluid Mech., 99, pp225.

[3] Berger, E. and Wille, R., 1972, Periodic flow phenomenon. *Ann. Rev. Fluid Mech.* 4, 313.

[4] Cantwell, B. and Coles, D., 1983, An Experimental study of entrainment and transport in the turbulent near wake of a circular cylinder. J. Fluid Mech., 136, pp321-374.

[5] Drain, L.E., *The Laser Doppler Technique,* John Wiley & Sons, Great Britain.

[6] Dryden, H.L. and Hill, G.C., 1930, Wind pressure on circular cylinders and chimneys, Bureau of Standards Journal of Research 5, pp. 653-693.

[7] Fage, A., Warsap, J.H., 1930, The effects of turbulence and surface roughness on the drag of a circular cylinder, ARC RM 1283.

[8] Gerich D. and Eckelmann H., 1982, Influence of end plates and free ends on the shedding frequency of circular cylinders. J.fluid. Mech. Vol. 122, pp109.

[9] Gould, R.W.F., et al., 1968, Proc. Symp. on Wind Effects on Buildings and Structures, pp10.

[10] Hölscher N. and Niemann H. J., 1987, Some aspects about the flow around a surface-mounted circular cylinder in a turbulent shear flow. Proceedings of 6th Symposium on Turbulent Shear Flows, Toulouse,7-9 September (1987).

[11] Kawamura,T. et al., 1984, Flow around a finite circular cylinder on a flat plate. Bull. JSME 27, p2142.

[12] Mair, W.A. and Maull, D.J., 1971, Bluff bodies and vortex shedding-a report on Euromech 17. J. Fluid Mech. 45, pp209.

[13] Morkovin, M.V., 1964, Flow around Circular Cylinder - A Kaleidoscope of Challenging Fluid Phenomenon, *Symposium on Fully Separated Flows(ASME)*, pp 102-118.

[14] Murlidhar, K. and Biswas G., 1996, *Advanced Engineering Fluid Mechanics*, Narosa Publishing House, India.

[15] Okamoto,T and Yagita, M., 1973, Bull. Japan. Soc. Mech. Engg., 16, p805.

[16] Roshko, A., 1961, Experiments on the flow past a circular at very high Reynolds number, J. Fluid Mech., Vol. 10, pp 345-356.

[17] Taniguchi, S. et al., 1981, Bull. JSME, 37, pp24-187.

[18] Wieselsberger. C., 1922, Phys. Zeits., Vol. 23, p219.

[19] Wille, R., 1960, Karman Vortex Streets. Adv. Appl. Mech. 6, pp273.